

A physically motivated ‘charge-exchange method’ for measuring electron temperatures within HII regions

Kathryn Kreckel¹, Oleg Egorov¹, Francesco Belfiore², Brent Groves³, Simon C. O. Glover⁴, Ralf R. Klessen^{4,5}, Karin Sandstrom⁶, Frank Bigiel⁷, Daniel A. Dale⁸, Kathryn Grasha⁹, Fabian Scheuermann¹, Eva Schinnerer¹⁰, and Thomas G. Williams¹⁰

¹ Astronomisches Rechen-Institut, Zentrum für Astronomie der Universität Heidelberg, Mönchhofstraße 12-14, D-69120 Heidelberg, Germany

e-mail: kathryn.kreckel@uni-heidelberg.de

² INAF – Osservatorio Astrofisico di Arcetri, Largo E. Fermi 5, I-50157, Firenze, Italy

³ International Centre for Radio Astronomy Research, University of Western Australia, 35 Stirling Highway, Crawley, WA 6009, Australia

⁴ Universität Heidelberg, Zentrum für Astronomie, Institut für Theoretische Astrophysik, Albert-Ueberle-Str 2, D-69120 Heidelberg, Germany

⁵ Universität Heidelberg, Interdisziplinäres Zentrum für Wissenschaftliches Rechnen, Im Neuenheimer Feld 205, D-69120 Heidelberg, Germany

⁶ Center for Astrophysics and Space Sciences, Department of Physics, University of California, San Diego, 9500 Gilman Drive, La Jolla, CA 92093, USA

⁷ Argelander-Institut für Astronomie, Universität Bonn, Auf dem Hügel 71, 53121 Bonn, Germany

⁸ Department of Physics and Astronomy, University of Wyoming, Laramie, WY 82071, USA

⁹ Research School of Astronomy and Astrophysics, Australian National University, Canberra, ACT 2611, Australia

¹⁰ Max-Planck-Institut für Astronomie, Königstuhl 17, D-69117, Heidelberg, Germany

Received XX; accepted XX

ABSTRACT

Aims. Temperature uncertainties plague our understanding of abundance variations within the ISM. Using the PHANGS-MUSE large program, we develop and apply a new technique to model the strong emission lines arising from H II regions in 19 nearby spiral galaxies at ~ 50 pc resolution and infer electron temperatures for the nebulae.

Methods. Due to the charge-exchange coupling of the ionization fraction of the atomic oxygen to that of hydrogen, the emissivity of the observed [O I] $\lambda 6300$ /H α line ratio can be modeled as a function of gas phase oxygen abundance (O/H), ionization fraction (f_{ion}) and electron temperature (T_e). We measure (O/H) using a strong line metallicity calibration, and identify a correlation between f_{ion} and [S III] $\lambda 9069$ /[S II] $\lambda 6716, 6730$, tracing ionization parameter variations.

Results. We solve for T_e , and test the method by reproducing direct measurements of T_e ([N II] $\lambda 5755$) based on auroral line detections to within ~ 600 K. We apply this *charge-exchange method* of calculating T_e to 4,129 H II regions across 19 PHANGS-MUSE galaxies. We uncover radial temperature gradients, increased homogeneity on small scales, and azimuthal temperature variations in the disks that correspond to established abundance patterns. This new technique for measuring electron temperatures leverages the growing availability of optical integral field unit spectroscopic maps across galaxy samples, increasing the statistics available compared to direct auroral line detections.

Key words. ISM:HII regions – ISM:abundances – galaxies:ISM – ISM:atoms – ISM: General – ISM: Clouds

1. Introduction

Star formation is regulated by the complex interplay of heating and cooling processes in the interstellar medium (ISM). The gaseous clouds that provide the raw materials for stars to form must cool sufficiently so that they can condense and collapse (McKee & Ostriker 2007; Klessen & Glover 2016). However, the resulting stars proceed to ionize and heat their surroundings, with the most massive stars contributing further mechanical energy and enriched materials at the end of their life via supernovae, feeding back into their natal environment (Maiolino & Mannucci 2019). This cycling of baryons on small scales is reflected by the temperature transitions from the dense cold molecular gas (~ 10 K) to the warm ionized medium ($\sim 10,000$ K) found

in H II regions, to the super-heated shock waves driven by supernova explosions ($\sim 10^6$ K).

In particular, within H II regions the electron temperature reflects not just the strength and hardness of the ionizing radiation field (O stars have temperatures up to $\sim 50,000$ K), but the ability of the gas to efficiently cool through collisionally excited lines arising from heavier elements (e.g., carbon, oxygen, nitrogen). In fact, the balance between heating and cooling in these nebulae reflects predominantly the metal abundance present in the surrounding ISM (Osterbrock & Ferland 2006), although age variations also play some role (Ho et al. 2019).

Direct measurement of electron temperatures is possible using faint temperature-sensitive emission lines. In the radio, it is possible to use radio recombination lines to derive the electron temperatures for H II regions, but these lines are very weak

and while such observations are possible for Milky Way targets (Balsler et al. 2015; Wenger et al. 2019; Pineda et al. 2019) they remain challenging for extragalactic targets (Zhao et al. 1996; Kempley et al. 2011; Luisi et al. 2018; Kewley et al. 2019). In the optical one can observe auroral lines (e.g. [O III] λ 4363, [N II] λ 5755, [S III] λ 6312, [O II] λ 7320,7330) in extragalactic systems, but they are also very faint, typically around $\sim 1\%$ of their strong line counterparts. Extensive long-slit observational projects have attempted to detect auroral lines across large samples of H II regions in nearby galaxies, but collecting statistically-significant samples of these faint lines is challenging. Observational campaigns targeting low-mass, metal-poor galaxies like M33, where the auroral lines are brighter, can accumulate relatively large numbers of detections (e.g., 61 H II regions with [O III] λ 4363 detections, Rosolowsky & Simon 2008), but this approach remains daunting for high-mass systems. In the CHemical Abundances of Spirals (CHAOS) project, initial results from Berg et al. (2020) detect auroral lines for a total of 190 H II regions across 4 galaxies, where they are able to make direct measurements of the electron temperatures.

With the advent of wide-field optical integral field spectrographs on large 8-meter class telescopes (e.g. VLT/MUSE and KCWI on Keck), it now becomes feasible to systematically observe much larger samples of H II regions with auroral line detections, but the telescope time requirements remain high. As part of the PHANGS-MUSE survey (Emsellem et al. 2022), four hours spent surveying NGC 1672 resulted in ~ 80 H II regions with [N II] λ 5755 auroral line detections (Ho et al. 2019). As such, direct detections of tens of auroral lines per galaxy have become feasible but expensive.

In addition to these auroral line measurements remaining extremely challenging, with only tens of H II regions we cannot uniformly sample the galaxy disks. Increased statistics on temperature (and metallicity) variations provides insights into the evolutionary processes regulating gas flows and galaxy evolution (Kreckel et al. 2019; Sánchez-Menguiano et al. 2019; Ho et al. 2019; Kreckel et al. 2020; Li et al. 2021), but remain plagued by the systematics affecting strong-line metallicities. We explore a new method to constrain the electron temperature, based on a combination of strong lines, with the goal of increasing the number of regions within which measurements of the electron temperature are possible. We present an overview of the physical motivation for the method in Section 2. We describe the data used in Section 3, and develop and validate our new method in Section 4. We discuss results in Section 5 and conclude in Section 6.

2. Physical Motivation for the Method

Nature has gifted us with a convenient coincidence. The ionization potential of oxygen (13.618 eV) is very similar to the ionization potential of hydrogen (13.598 eV). As such, the charge-exchange reaction $O^0 + H^+ \leftrightarrow O^+ + H^0$ is very efficient, and acts to couple the ionization fraction of oxygen to the ionization fraction of hydrogen (see, e.g. Draine 2011; Tielens 2010). This means that the number densities (which we denote as $n(X)$, for species X) of oxygen and hydrogen are related by

$$\frac{n(O^0)}{n(O)} \approx \frac{n(H^0)}{n(H)}, \quad (1)$$

where

$$n(H) \equiv n(H^0) + n(H^+) \quad (2)$$

and

$$n(O) \equiv n(O^0) + n(O^+) \quad (3)$$

Note that we define the ionization fraction of hydrogen as

$$f_{\text{ion}} \equiv \frac{n(H^+)}{n(H)} = \frac{n(H^+)}{n(H^+) + n(H^0)} = \frac{n(H^+)/n(H^0)}{n(H^+)/n(H^0) + 1}. \quad (4)$$

Therefore, for line emission associated with the relevant ions,

$$\frac{[\text{O I}]\lambda 6300}{H\alpha} \propto \frac{n(O^0)}{n(H^+)} = \frac{n(O)}{n(H)} \frac{n(H^0)}{n(H^+)} = \frac{n(O)}{n(H)} \frac{1 - f_{\text{ion}}}{f_{\text{ion}}} \quad (5)$$

This is significant as the line ratio [O I]/H α depends only on temperature (through the proportionality pre-factor), metallicity ($n(O)/n(H)$) and the ionization fraction of hydrogen (f_{ion}).

Using the latest calculations of the [O I] and H α emission rates (Barklem 2007; Dong & Draine 2011), we derive the emissivity of [O I] λ 6300 relative to H α (as outlined in Appendix A) to be

$$\begin{aligned} \frac{[\text{O I}]\lambda 6300}{H\alpha} &= 8492 \frac{f_{\text{OI}}(T)}{T_4^{-0.942 - 0.031 \ln T_4}} \exp\left(-\frac{2.284}{T_4}\right) \\ &\times \frac{n(O)}{n(H)} \\ &\times \frac{n(H^0)}{n(H^+)} \xi \end{aligned} \quad (6)$$

where T_4 is the electron temperature (T_e) in units of 10,000 K, f_{OI} is defined as

$$f_{\text{OI}}(T) = \sum_{i=0}^6 a_i T_4^i \quad (7)$$

where the coefficients a_i are listed in Table 1, and ξ is a function of the hydrogen ionization ratio

$$\xi = \frac{1 + n(H^0)/n(H^+)}{\frac{8}{9} + n(H^0)/n(H^+)}. \quad (8)$$

This factor ξ is just above unity and ranges from 1 to 9/8. This equation holds if the [O I] and H α emission are co-spatial, arising from the same parcel of gas. We discuss this in more detail below, and explore the implications of this assumption in Section 5.3.1. This is an update to the relation provided in Reynolds et al. (1998).

The aim of this paper is to utilize a measurement of [O I]/H α , combined with an estimate of f_{ion} , to infer T_e . While T_e can be directly measured through the detection of faint auroral lines, there exist no well-established prescriptions to infer f_{ion} from observations of strong lines. In this paper, we determine an empirical relation between f_{ion} and strong line diagnostic ratios in

Table 1. Coefficients for Equation 7.

Coefficient	Value
a_0	-1.00
a_1	+6.4854011
a_2	-4.17358515
a_3	+1.81446389
a_4	-0.514022051
a_5	+8.39069326 $\times 10^{-2}$
a_6	-5.93343677 $\times 10^{-3}$

order to allow us to solve for T_e . This *charge-exchange method* of determining T_e represents a novel approach which may be widely applicable to existing data sets. We develop our method using a set of line fluxes measured arising from integrated H II regions, as extragalactic H II regions are generally unresolved.

For this charge-exchange method to apply, we assume that electron collisions dominate the excitation of the [O I] line, rather than collisions with atomic hydrogen. The critical fractional ionization above which electron collisions dominate is $\sim 10^{-3}$ – 10^{-4} , which we expect to be true for the H II regions we consider. We also assume that the emitting regions are in the low density limit, rather than the local thermodynamic equilibrium limit. Since the critical density is $\sim 10^6 \text{ cm}^{-3}$, this should also be valid for all of the H II regions we consider.

There are limitations to this method that are worth highlighting here, and that will be addressed in more detail in Section 5.2. This model compares the [O I] and H α line emission. However, while the majority of the hydrogen in an H II region is ionized and emitting in H α , [O I] will be emitted mainly in an outer shell near the ionization front. In applying this method, we are assuming that T_e is uniform across both the H α and [O I] emitting regions. Ideally, we would further consider emission that is co-spatial, arising from the same parcel of gas. However, for unresolved H II regions, we can consider only emission integrated across the entire nebula. In our approach, we argue that f_{ion} constrains the size of the partially ionized zone, accounting for this discrepancy in emitting zones. Over larger (kpc scale) regions of the diffuse ionized gas, the radiation field is more diluted (low ionization parameter) and therefore the partially ionized zone is wider and would lead to a better correspondence between H α and [O I] emitting regions.

This technique was initially developed in relation to diffuse ionized gas in the Milky Way (Reynolds et al. 1998), and later applied to four individual H II regions in the Milky Way (Hausen et al. 2002). We further develop this method, and aim to apply it to the thousands of H II regions within the PHANGS-MUSE sample. [O I] emission can be challenging to measure, as it is faint and can be blended with the strong and highly variable telluric airglow emission. In this work we target nearby (~ 10 – 20 Mpc) galaxies with sufficiently large velocity offset from terrestrial [O I], and with sufficient depth to detect [O I] across a wide sample of H II regions. Here, we explore the regime where an entire H II region is integrated over 50–100 pc scales. While the main goal is to infer T_e , we note that we need to assume a metallicity in order to apply the charge exchange method. Therefore, our T_e measurement is dependent on the assumed strong-line metallicity, and using it to infer metallicities using the direct method would be circular. We test the metallicity dependence of the method in Section 4.4. Some iterative approach may be suitable, but this is beyond the scope of this work.

3. Data

3.1. CHAOS

To develop our method, we explored data from the CHAOS project. Berg et al. (2020) summarizes the latest results (see also Berg et al. 2015; Croxall et al. 2015, 2016), including four galaxies (NGC 628, NGC 3184, M 51 and M 101) with a total of 190 H II regions with auroral line detections as measured from integrated H II region spectra. Of these, 121 have detections of [N II] $\lambda 5755$, 131 have [S III] $\lambda 6312$, 154 have [O II] $\lambda 7320, 7330$, and 72 have [O III] $\lambda 4363$. These auroral lines, arising from high energy levels, are used in combination with the nebular lines

from lower energy levels of the same ion to compute electron temperatures for each ion. Using different ions to represent different temperatures across ionization zones in the nebulae, Berg et al. (2020) combined these measurements to compute the oxygen abundance, $12 + \log(\text{O}/\text{H})$, using the direct method. In this way, from the CHAOS data set, we have measurements of T_e and O/H for 190 H II regions, as well as a full catalog of strong emission lines ([O II] $\lambda 3727, 3729$, [O III] $\lambda 5007$, H β , [O I] $\lambda 6300$, [N II] $\lambda 6583$, H α , [S II] $\lambda 6716, 6730$ and [S III] $\lambda 9069$). All line fluxes from their catalog have been corrected for extinction using the Balmer series (H α , H β).

These observations were carried out using the Multi-Object Double Spectrographs (MODS; Pogge et al. 2010) with slit masks on the Large Binocular Telescope (LBT). Slits placed on individual H II regions were designed to be $1''$ wide and $10''$ long. This slit-width is well matched to the seeing during observations, however as the brightest H II regions are typically selected this does not necessarily encompass the full H II region size, which for giant H II regions can be as large as ~ 100 pc (Azimlu et al. 2011; Mannucci et al. 2021). At the 7–11 Mpc distances of the four targets this slit-width corresponds to $1'' = 30$ – 50 pc, such that some slit losses may be expected. No correction is applied to account for the local diffuse ionized gas (DIG) background emission.

3.2. PHANGS-MUSE

After initial investigations into the charge-exchange method using the CHAOS data, we develop and test our method using H II regions selected from the PHANGS-MUSE dataset (Emsellem et al. 2022, Groves et al. in prep). The Physics at High Angular resolution in Nearby Galaxies (PHANGS) collaboration has targeted nearby spiral disk galaxies along the star-forming main sequence (Table 2). Targets were selected to be nearby ($D < 19$ Mpc, $1'' < 100$ pc) and moderately inclined (inclination $< 60^\circ$). Observations of 19 galaxies were carried out using the Very Large Telescope/Multi Unit Spectroscopic Explorer (VLT/MUSE; Bacon et al. 2010) instrument primarily as part of a MUSE large program (PI: Schinnerer), which observed 172 individual MUSE pointings across these 19 galaxies over 4800–9300 Å at $< 1''$ resolution. The data reduction pipeline and data analysis pipeline used to reduce this data set and extract emission line maps are described in detail in Emsellem et al. (2022). This results in an optical integral field spectroscopic data cube, as well as integrated line emission maps of a wide range of both strong ([O III] $\lambda 5007$, H β , [O I] $\lambda 6300$, [N II] $\lambda 6583$, H α , [S II] $\lambda 6716, 6730$, [S III] $\lambda 9069$) and auroral ([N II] $\lambda 5755$, [S III] $\lambda 6312$, [O II] $\lambda 7320, 7330$) emission line fluxes. For the [O III] and [N II] doublets we measure only the stronger line, and for the [S III] doublet we measure only the bluer line, and assume fixed atomic ratios (Osterbrock & Ferland 2006; Tayal et al. 2019) as

$$\begin{aligned} [\text{O III}]\lambda 4958 &= 0.35 \times [\text{O III}]\lambda 5007 \\ [\text{N II}]\lambda 6548 &= 0.34 \times [\text{N II}]\lambda 6584 \\ [\text{S III}]\lambda 9532 &= 2.5 \times [\text{S III}]\lambda 9069 \end{aligned} \quad (9)$$

Using the H α emission line maps, Santoro et al. (2022) morphologically identified individual nebular regions using the `NIIPHOT` package (Thilker et al. 2000), using a technique similar to that described in Kreckel et al. (2019). This works by identifying peaks in the H α distribution, and growing those peaks until a neighboring region is encountered or a termination criterion set by the flux gradient is reached. These nebular region

Table 2. Properties of the galaxies in the PHANGS-MUSE sample

Name	Type	Dist ^a [Mpc]	$r_{\text{eff}}^{\text{b}}$ [arcsec]	Inclination ^c [deg]	Pos Angle ^c [deg]	$M_{\text{star}}^{\text{b}}$ [M_{\odot}]	$E(B - V)_{\text{MW}}^{\text{d}}$ [mag]	$v_{\text{sys}}^{\text{b}}$ [km/s]
NGC 0628	Sc	9.8	82	8	20	2.2e+10	0.06	650
NGC 1087	Sc	15.9	42	42	359	8.6e+09	0.03	1501
NGC 1300	Sbc	19.0	71	31	278	4.1e+10	0.03	1545
NGC 1365	Sb	19.6	195 ^e	55	201	9.8e+10	0.02	1613
NGC 1385	Sc	17.2	40	44	181	9.5e+09	0.02	1476
NGC 1433	SBa	18.6	48	28	199	7.3e+10	0.01	1057
NGC 1512	Sa	18.8	52	42	261	5.2e+10	0.01	871
NGC 1566	SABb	17.7	37	29	214	6.1e+10	0.01	1483
NGC 1672	Sb	19.4	36	42	134	5.4e+10	0.02	1318
NGC 2835	Sc	12.2	56	41	1	1.0e+10	0.09	867
NGC 3351	Sb	10.0	63	45	193	2.3e+10	0.02	774
NGC 3627	Sb	11.3	66	57	173	6.8e+10	0.03	715
NGC 4254	Sc	13.1	38	34	68	2.7e+10	0.03	2388
NGC 4303	Sbc	17.0	42	23	312	3.3e+10	0.02	1559
NGC 4321	SABb	15.2	75	38	156	5.6e+10	0.02	1572
NGC 4535	Sc	15.8	82	44	179	3.4e+10	0.02	1953
NGC 5068	Sc	5.2	78	35	342	2.5e+09	0.09	667
NGC 7496	Sb	18.7	42	35	193	9.9e+09	0.01	1639
IC 5332	SABc	9.0	83	26	74	4.7e+09	0.01	699

Adopted from the PHANGS sample table (v1p6; Leroy et al. 2021)

^a from Anand et al. (2021)

^b from Leroy et al. (2021)

^c from Lang et al. (2020)

^d from Schlafly & Finkbeiner (2011)

^e Due to AGN bias, derived from the scale length (l_*) as $r_{\text{eff}} = 1.41 l_*$ following Equation 5 in Leroy et al. (2021).

masks are then applied to the original data cube, and the spectra within each nebular region are summed and re-fit using the data analysis pipeline. The resulting nebular catalog compiles a list of objects with their associated line fluxes, extinction corrected using the Balmer decrement, with approximately 31,000 regions identified across the full sample. All galaxies are at sufficiently high systemic velocities ($v_{\text{sys}} > 650 \text{ km s}^{-1}$) that the critical [O I] emission line is not blended with telluric airglow (Table 2).

We apply the standard BPT (Baldwin et al. 1981) diagnostic diagrams requiring $S/N > 3$ in all relevant lines, and construct our H II region catalog by selecting those regions from the nebular catalog which are consistent with both of the photoionization demarcations given by Kauffmann et al. (2003) in the [O III]/H β vs. [N II]/H α diagram and the Kewley et al. (2001) lines in the [O III]/H β vs. [S II]/H α diagram. Regions that have $S/N < 3$ in any of the relevant diagnostic lines are excluded from the sample. We further exclude H II regions within one $1''$ of the field edge or a foreground star. This results in an H II region catalog consisting of $\sim 24,000$ objects. Given that the median size of our H II regions is approximately consistent with our seeing limit, we expect that most of these H II regions are unresolved. In this sense, we always contain the full spatial extent of the H II region in our integrated spectrum.

The PHANGS-MUSE spectra also include detections of the faint [N II] $\lambda 5755$ auroral line (Ho et al. 2019). Fitting of this faint line (typically less than 1% of the H α line flux) is carried out using the integrated H II region spectra, subtracting the stellar population fit, and performing a Gaussian fit on the residual. Given the faintness of the line, very slight offsets in the stellar population fitting can result in systematic residuals at the location of the [N II] line. To improve the flux estimate from our Gaussian fit, we fix the velocity centroid to have the same systemic velocity as we measure for the brighter H α line, but additionally allow for a local linear background to account for systematics in the stellar population fit. Errors are determined

by sampling the error spectrum and repeating this analysis 100 times. This results in ~ 840 H II regions where the [N II] $\lambda 5755$ line is detected at $S/N > 10$. As with the other measured lines, we correct for extinction in using the Balmer decrement, combine this with the dereddened measurement of [N II] $\lambda 6583$ and use PYNEB (Luridiana et al. 2015) assuming $n_e = 10 \text{ cm}^{-3}$, consistent with the measured values (Barnes et al. 2021), to compute $T_e(\text{[N II]})$.

For the fainter and unresolved regions the DIG background may introduce uncertainties in recovering the intrinsic line fluxes. In order to measure the DIG contribution at the position of each H II region, we mask out all nebular regions and compute the median line flux within a $10'' \times 10''$ box around each region for the lines most strongly emitted by the DIG (H β , [O I], H α , [N II], [S II]). We require a 3σ detection of a DIG signal in order to include it in our calculations. As implementing the DIG subtraction is a fairly uncertain process, we do not attempt any DIG subtraction. Instead, we aim to minimize the impact of the DIG on our measurements by requiring that H II regions have a $> 50\%$ contrast of all lines against the surrounding DIG background. Approximately 35% of all H II regions do not have significant detections in all necessary emission lines against the DIG background, and are excluded from further analysis.

3.3. Strong line O/H abundances

As this method relies on knowing O/H, we apply a strong line abundance prescription to both the CHAOS and PHANGS H II region catalogs. Our preferred strong line abundance prescription is the S calibration from Pilyugin & Grebel (2016), an empirical method that relies on the combination of three diagnostic line ratios. This provides an improved ability to remove degeneracies between metallicity and ionization parameter when compared to prescriptions that use only one or two diagnostic ratios (for some discussion see Ho 2019 and Kreckel et al. 2019). It

has been shown to produce qualitatively similar results to the Dopita et al. (2016) N2S2 prescription (Kreckel et al. 2019), and achieves small systematic uncertainties (Metha et al. 2021).

The S calibration relies on the following three standard diagnostic line ratios:

$$\begin{aligned} N_2 &= ([N\text{ II}]\lambda 6548 + \lambda 6584)/H\beta, \\ S_2 &= ([S\text{ II}]\lambda 6717 + \lambda 6731)/H\beta, \\ R_3 &= ([O\text{ III}]\lambda 4959 + \lambda 5007)/H\beta. \end{aligned} \quad (10)$$

The prescription is defined separately over the upper and lower branches in $\log N_2$. The upper branch ($\log N_2 \geq -0.6$) is calculated as

$$\begin{aligned} 12 + \log(O/H) &= 8.424 + 0.030 \log(R_3/S_2) + 0.751 \log N_2 \\ &+ (-0.349 + 0.182 \log(R_3/S_2) + 0.508 \log N_2) \\ &\times \log S_2 \end{aligned} \quad (11)$$

and the lower branch ($\log N_2 < -0.6$) is calculated as

$$\begin{aligned} 12 + \log(O/H) &= 8.072 + 0.789 \log(R_3/S_2) + 0.726 \log N_2 \\ &+ (1.069 - 0.170 \log(R_3/S_2) + 0.022 \log N_2) \\ &\times \log S_2 \end{aligned} \quad (12)$$

4. Method development

Using the four galaxies in the CHAOS dataset, we begin by using their measured $[O\text{ I}]/H\alpha$, T_e based on auroral line detections, and direct method metallicity in order to infer f_{ion} for each of their H II regions (Figure 1). This direct method metallicity is derived by associating different T_e values to different ionization zones in the nebula, such that the final metallicity is not independent of the T_e measurements. Using the S calibration to derive metallicities provides similar results, although with increased scatter. Based on the auroral line detections of $[N\text{ II}]$, $[O\text{ II}]$, $[O\text{ III}]$, and $[S\text{ III}]$ this approach provides four different measurements of T_e , reflecting the ionic temperature in the zone where each ion is dominant. We find f_{ion} values ranging from 0.93 to 0.99, and a median value of $f_{\text{ion}}=0.97$ across all H II regions.

As we are integrating over the entire H II region, although $[O\text{ I}]$ is not emitted throughout the entire nebula, we expect that f_{ion} will change systematically with the ionization structure of the nebulae and the size of the partially ionized region. To that end, we look for correlations with line ratios that depend on changes in the ionization parameter

$$q \equiv \frac{Q(H^0)}{4\pi R^2 n(H)}, \quad (13)$$

where $Q(H^0)$ is the number of ionizing photons emitted per second, R is the distance between the central source and the emitting material and $n(H)$ is the hydrogen density. In photoionization models, the ionization parameter q correlates linearly with the log of $[O\text{ III}]/[O\text{ II}]$, $[S\text{ III}]/[S\text{ II}]$, and $[O\text{ III}]/H\beta$, with both $[O\text{ III}]/[O\text{ II}]$ and $[O\text{ III}]/H\beta$ showing additional dependences on metallicity (Kewley & Dopita 2002; Dors et al. 2011). Note that here we define:

$$\begin{aligned} [O\text{ III}]/[O\text{ II}] &\equiv [O\text{ III}]\lambda 5007/[O\text{ II}]\lambda 3726, 3729 \\ [S\text{ III}]/[S\text{ II}] &\equiv [S\text{ III}]\lambda 9069, 9532/[S\text{ II}]\lambda 6717, 6731 \\ [O\text{ III}]/H\beta &\equiv [O\text{ III}]\lambda 5007/H\beta. \end{aligned} \quad (14)$$

We find a strong correlation between f_{ion} and $[S\text{ III}]/[S\text{ II}]$ (as a proxy for ionization parameter) for all four ions (Figure 1), with $T_e([N\text{ II}])$ producing the strongest correlation (as judged by the Spearman's rank correlation coefficient, $\rho=0.67$). This is reasonable, as the temperature of the ion tracing the low-ionization

zone of the nebula is best suited to describe the $[O\text{ I}]$ emitting region (Berg et al. 2020; see also Section 5.2). It also shows the most uniform trend across all four galaxies in the sample. Given the strong correlation and relatively high number of detections, we choose to adopt $T_e([N\text{ II}])$ as a reference temperature for the rest of the analysis in this paper.

Weaker correlations are seen with $[O\text{ III}]/H\beta$ or $[O\text{ III}]/[O\text{ II}]$ ($\rho \sim 0.5$, Figure 2). Some correlations are also seen with the input parameters used in calculating f_{ion} (Figure 3), showing the strongest correlation with $[O\text{ I}]/H\alpha$ ($\rho=-0.57$) and a weaker correlation with $T_e([N\text{ II}])$ ($\rho=0.24$). No significant correlation is seen with $12+\log(O/H)$, suggesting f_{ion} is relatively insensitive to changes in abundance.

4.1. Aperture biases

While the CHAOS data set presents a remarkable catalog of emission lines and derived properties, by design it is targeting only the central regions of the brightest H II regions in order to improve the chances of detecting the faint auroral lines. We note that in Figure 1, the majority of CHAOS H II regions have $[S\text{ III}]/[S\text{ II}] > 1.0$. These are relatively high compared to what is reported in samples that probe fainter H II regions (e.g. Kreckel et al. 2019; Mingozzi et al. 2020). In particular, the incomplete spatial coverage of any given H II region results in an inherent bias for line ratio diagnostics that show radial structure within a H II region. This is apparent in the $[S\text{ III}]/[S\text{ II}]$ line ratio, as CHAOS observations probe only the central ~ 50 pc ($\sim 1''$) of the nebulae, where the $[S\text{ III}]$ emission is strongest, and miss $[S\text{ II}]$ emission in the outer nebulae (see also Mannucci et al. 2021).

We demonstrate this directly by cross matching the H II regions cataloged by CHAOS and by PHANGS-MUSE in NGC 628, the only galaxy contained in both samples. As CHAOS is predominantly targeting the outer disk while PHANGS-MUSE is limited to the inner disk, only 13 H II regions overlap between the two samples. In Figure 4 we compare the $[S\text{ III}]/[S\text{ II}]$ line ratios, and demonstrate how the aperture bias results in systematically higher measurements in the CHAOS sample. This offset persists even when accounting for differences in the assumed reddening $E(B-V)$ (due to both the foreground Milky Way and local reddening within the galaxy) adopted in the two surveys. Challenges such as this motivate our use of integrated H II region spectra for this paper, but similarly prevent us from relying solely on the CHAOS sample for the determination of an empirical relation between f_{ion} and $[S\text{ III}]/[S\text{ II}]$.

Of the 13 H II regions, only 11 have detections of $[N\text{ II}]\lambda 5755$, and subsequent calculations of $T_e([N\text{ II}])$, in both samples. In Figure 5 we show a comparison of the derived $T_e([N\text{ II}])$, which follows very well the one-to-one line within the uncertainties. This agreement speaks to a smooth and roughly constant temperature structure within the $[N\text{ II}]$ emitting region, as expected, as well as the high fidelity in both data sets.

4.2. Parameterizing f_{ion}

From the CHAOS sample, it is clear that changing the size of the partially ionized zone within the H II region corresponds to a change in ionization parameter, with the strongest correlation identified between f_{ion} when measured using $T_e([N\text{ II}])$, and $[S\text{ III}]/[S\text{ II}]$ (as a proxy for ionization parameter). As expected from models, the ionisation fraction (i.e. basically the extent of the partially ionised zone) correlates with ionisation parameter. However, given the aperture bias, we cannot employ the

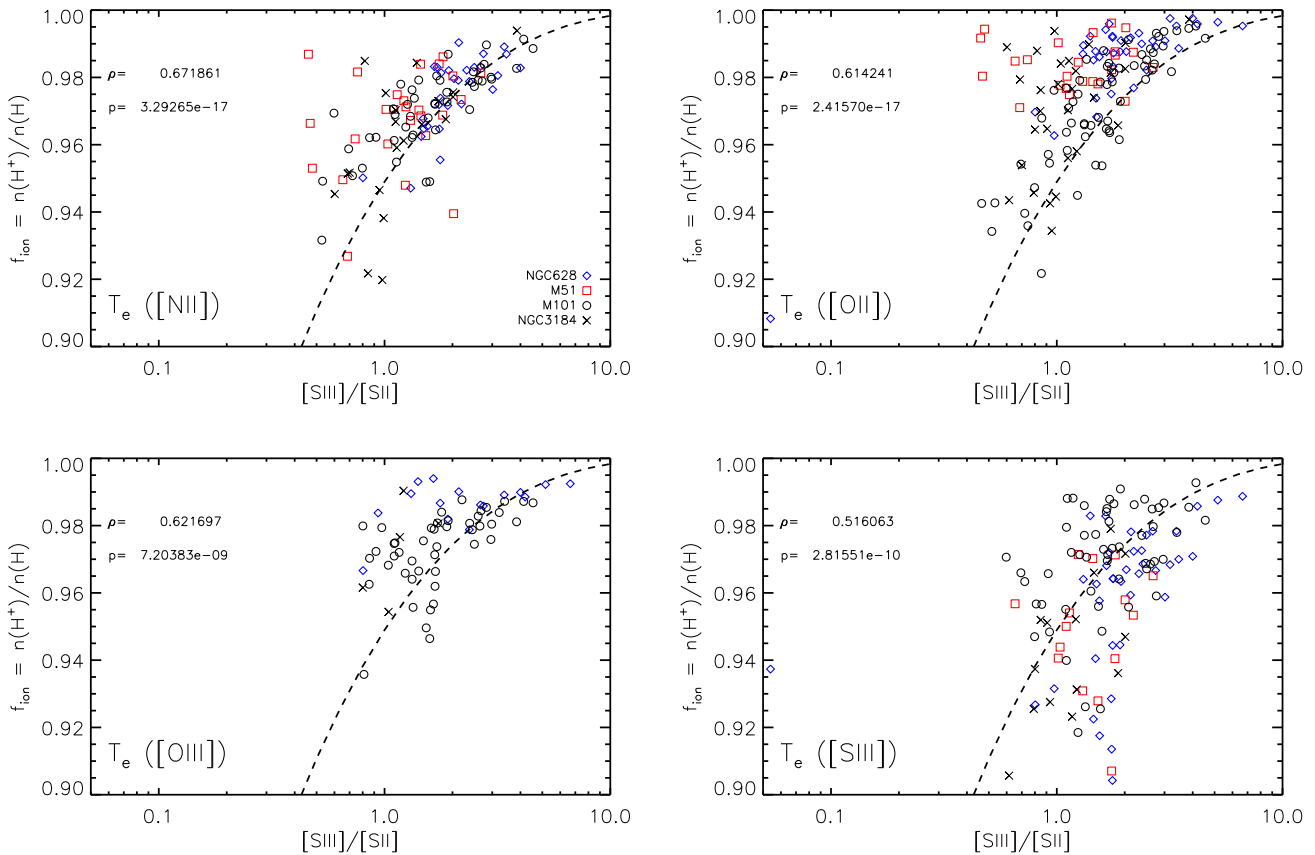


Fig. 1. For the CHAOS H II regions, we model f_{ion} based on Equation 6, assuming different input electron temperatures based on auroral line measurements ($T_e([\text{N II}])$, $T_e([\text{O II}])$, $T_e([\text{O III}])$, $T_e([\text{S III}])$) as well as their reported $12+\log(\text{O}/\text{H})$ and $[\text{O I}]/\text{H}\alpha$. Each of the four galaxies is shown with separate symbols, and the Spearman’s rank correlation coefficient (ρ) and its significance (p) are shown in each figure. Each value of f_{ion} is plotted as a function of the $[\text{S III}]/[\text{S II}]$ line ratio, which robustly traces changes in the ionization parameter (Kewley & Dopita 2002). We identify $T_e([\text{N II}])$ as showing the strongest correlation ($\rho = 0.69$) and a large number of detections, and therefore choose to adopt $T_e([\text{N II}])$ as a reference temperature for the rest of the analysis in this paper. The dashed line shows the fit derived in Section 4.2, using a combination of PHANGS-MUSE and CHAOS H II regions. This same line is overplotted for the other panels (dashed lines) to allow comparison across the ionic temperatures.

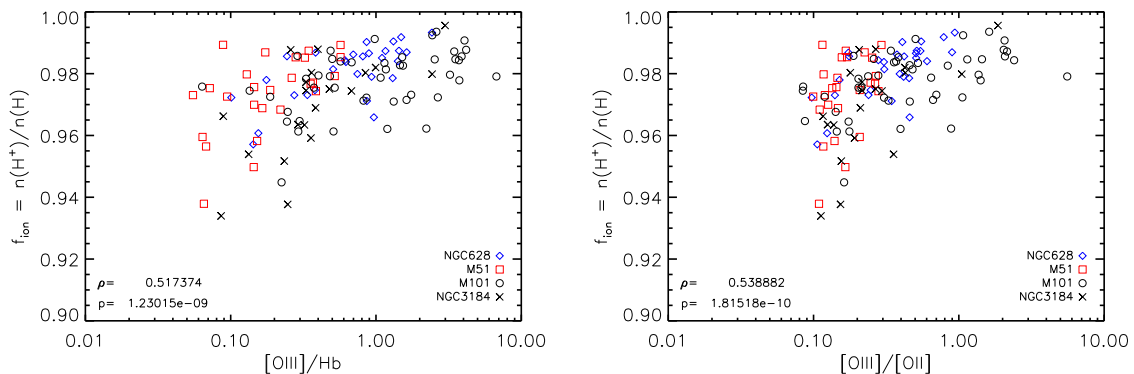


Fig. 2. We demonstrate further (weaker) correlations between f_{ion} and line ratios tracing changes in ionization parameter ($[\text{O III}]/\text{H}\beta$, left; $[\text{O III}]/[\text{O II}]$, right) for H II regions in the CHAOS sample, using $T_e([\text{N II}])$ as our fiducial temperature measurement. Each of the four galaxies is shown with separate symbols, and the Spearman’s rank correlation coefficient (ρ) and its significance (p) are shown in each figure. Weaker correlations are seen ($\rho \sim 0.5$) compared to the correlations with $[\text{S III}]/[\text{S II}]$ (Figure 1).

measurements of $[\text{S III}]/[\text{S II}]$ from CHAOS when determining an empirical relation. We therefore use the 840 H II regions from PHANGS-MUSE which have $T_e([\text{N II}])$ measurements to determine an empirical relation, such that we can use the observed $[\text{S III}]$ and $[\text{S II}]$ emission to constrain f_{ion} . With this prescription

we will then be able to measure all three necessary parameters (f_{ion} , $12+\log(\text{O}/\text{H})$ and $[\text{O I}]/\text{H}\alpha$) using strong line methods and thus solve for T_e .

In Figure 6 we show f_{ion} as a function of $[\text{S III}]/[\text{S II}]$ for the full PHANGS-MUSE H II region sample (points). We impose

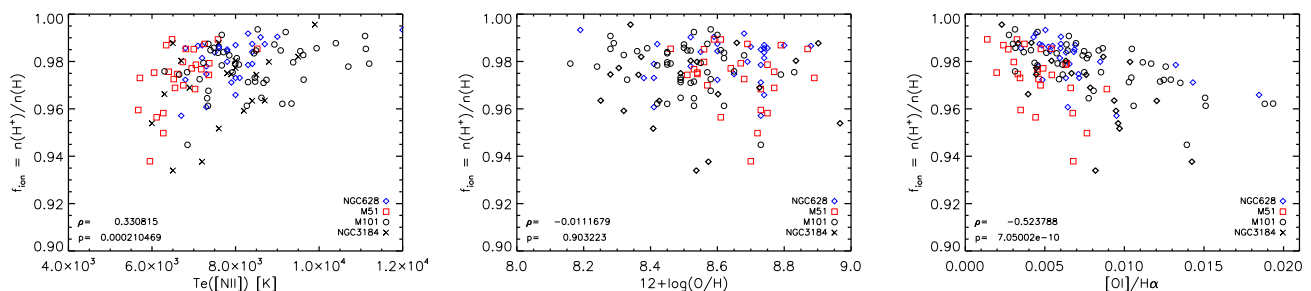


Fig. 3. Correlating f_{ion} with the three input parameters ($T_e(\text{N II})$, $12+\log(\text{O}/\text{H})$, $[\text{O I}]/\text{H}\alpha$) for each H II region in the CHAOS sample. Each of the four galaxies is shown with separate symbols, and the Spearman's rank correlation coefficient (ρ) and its significance (p) are shown in each figure. The f_{ion} variations correlate most strongly with changes in $[\text{O I}]/\text{H}\alpha$, but show a weaker correlation than the trends with $[\text{S III}]/[\text{S II}]$ in Figure 1.

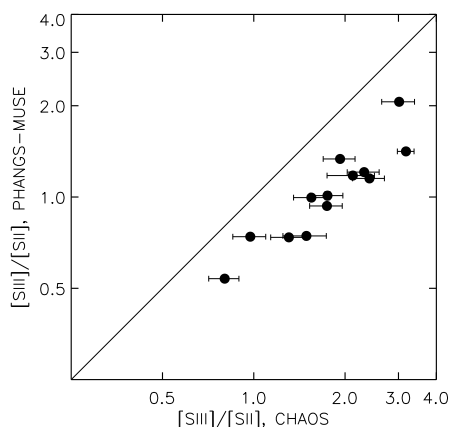


Fig. 4. Comparison of the $[\text{S III}]/[\text{S II}]$ line ratio measured across integrated H II region spectra from PHANGS-MUSE with the measurement obtained within the CHAOS 1'' slit for 13 H II regions that overlap between the two surveys. Error bars are shown for both surveys, although the PHANGS errors are smaller than the symbols. The one-to-one line (black) shows that CHAOS systematically overestimates the line ratio by focusing on only the central brightest part of these extended H II regions, where the $[\text{S III}]$ emission is preferentially located. This demonstrates the challenges of applying such resolved measurements to broader H II region samples.

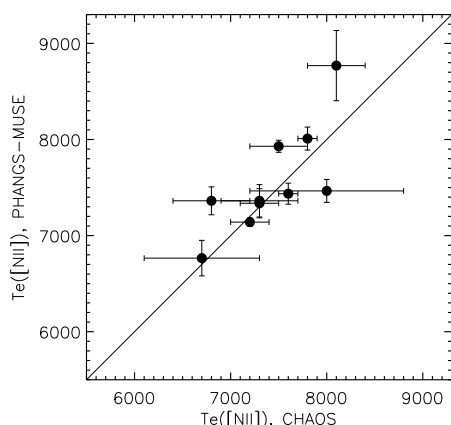


Fig. 5. Comparison of $T_e(\text{N II})$ measured in integrated H II region spectra from PHANGS-MUSE with equivalent measurements from the CHAOS 1'' slit for 10 H II regions that have reported $[\text{N II}]\lambda 5755$ line detection in both surveys. We observe good systematic agreement between the two measurements.

the requirement that regions be detected against the DIG background by at least a 50% contrast, and consider only regions with $[\text{S III}]/[\text{S II}] > 0.5$, where our sample appears more complete (filled circles). We also show the H II regions from all four galaxies from the CHAOS sample (open circles), which due to aperture biases have systematically overestimated $[\text{S III}]/[\text{S II}]$ line ratios compared to the MUSE data (see Figure 4), but nonetheless form a nearly continuous sequence with the PHANGS-MUSE H II regions. Given the non-linear shape in this relation, it is apparent that a linear extrapolation from the CHAOS measurements (preferentially biased to high $[\text{S III}]/[\text{S II}]$) would not be suitable for the bulk of the PHANGS-MUSE sample (seen also in Figure 1). However, given the smooth transition across samples, this also suggests that the correlation holds even when considering changes in f_{ion} and changes in ionization parameter within the nebulae. To determine the most widely-applicable fit, we combine the PHANGS-MUSE and CHAOS samples and construct bins in $[\text{S III}]/[\text{S II}]$ requiring a minimum of 10 data points, to demonstrate the median trend across the sample (red line, Figure 6). To this median trend, we fit a third order power law where we have fixed the asymptote to $f_{\text{ion}}=1.0$. This shows very good agreement with the binned median, and is parameterized by

$$f_{\text{ion}} = 1.0 + c_1 \times (\log_{10}([\text{S III}]/[\text{S II}]) - c_2)^3, \quad (15)$$

where $c_1 = 0.0139 \pm 0.0060$ and $c_2 = 1.4119 \pm 0.1890$.

We further overplot this fit on the relations in Figure 1 for the CHAOS data, and see reasonable agreement with many of the different ionic temperatures. The trend is reasonably consistent with $T_e(\text{N II})$, $T_e(\text{S III})$, and $T_e([\text{O III}])$, but clearly offset from $T_e([\text{O II}])$. This reflects some of the previously reported discrepancies between different ionization zones (Berg et al. 2020), though it is somewhat surprising that $[\text{O III}]$ (a very high ionisation tracer) would work better than e.g. $[\text{O II}]$ (a low-ionisation tracer).

Given that we have imposed a minimum value of $[\text{S III}]/[\text{S II}] > 0.5$, we cannot extrapolate this relation to lower $[\text{S III}]/[\text{S II}]$ without additional data or modeling. We revisit this decision in Section 5.3.

4.3. Method summary

We summarize here the conditions that must be met in order to apply the charge-exchange method. Motivation for these choices is detailed at the beginning of Section 4. When modeling T_e based on integrated line fluxes within H II regions:

- We require $\text{S/N} > 10$ in all of the following emission lines: $\text{H}\beta$, $[\text{O III}]$, $\text{H}\alpha$, $[\text{N II}]$, $[\text{S II}]$, $[\text{S III}]$. We use a fairly high

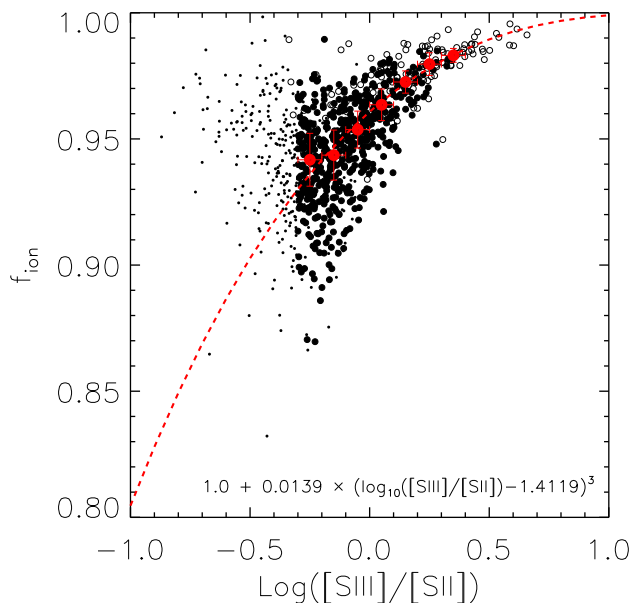


Fig. 6. As in Figure 1, we model f_{ion} assuming the values of $T_e(\text{[N II]})$ measured from direct detection of auroral lines in the PHANGS-MUSE H II region sample (points). This forms a continuous sequence with the H II regions in the CHAOS sample (open circles), but with a significantly more pronounced non-linear trend. From the PHANGS-MUSE sample, we select only regions with more than 50% contrast against the DIG background and with $[\text{S III}]/[\text{S II}] > 0.5$ (filled circles). We then combine the PHANGS-MUSE and CHAOS samples to construct a binned median (red circles). We fit this with the functional form described in Equation 15 (red dashed line) to determine our empirical relation for f_{ion} .

threshold as the errors are underestimated by an estimated $\sim 40\%$ (Emsellem et al. 2022).

- We require a contrast of $>50\%$ against the DIG background for each line.
- We require $[\text{S III}]/[\text{S II}] > 0.5$.
- We correct all lines for attenuation using the Balmer decrement.
- We calculate the $[\text{O I}]/\text{H}\alpha$ line ratio.
- We calculate $12+\log(\text{O}/\text{H})$ following the Pilyugin & Grebel (2016) S-calibration, as in Equations 11 and 12.
- We calculate f_{ion} from the $[\text{S III}]/[\text{S II}]$ line ratio, as in Equation 15.
- We use these three values to solve Equation 6 for T_e .

4.4. Validation

In Figure 7 we validate our charge-exchange method by applying it to the 531 PHANGS-MUSE H II regions that meet the criteria in Section 4.3 and have $T_e(\text{[N II]})$ derived from auroral line methods. We find a high correlation (Spearman’s rank correlation coefficient $\rho=0.79$), good systematic agreement (~ 6 K) and relatively small scatter (~ 550 K) between the direct-method and “charge-exchange method” measurements of T_e . Here, the scatter is calculated as the dispersion relative to the auroral line measurement, neglecting any absolute offset. Requiring a higher contrast of 300% against the DIG background reduces the H II region sample by a factor of ~ 2 but does not significantly change these statistics. On the other hand, using a fixed value for $f_{\text{ion}}=0.94$

(the median for the PHANGS-MUSE sample) introduces a significant scatter (~ 800 K) and non-linearity to the relation. Employing the variable f_{ion} but relaxing our assumption on how the metallicity is determined (either via a fixed linear radial gradient or a fixed global value for each galaxy) retains a high degree of correlation ($\rho \sim 0.78$) and only slightly higher scatter (~ 600 K). This demonstrates the relative insensitivity of this method to the input metallicity, though we note that our galaxies cover a fairly limited metallicity range of $8.3 < 12+\log(\text{O}/\text{H}) < 8.7$ (Santoro et al. 2022).

We perform an additional validation of our various assumptions by applying this charge-exchange method next to the CHAOS data set, adjusting the different assumptions we make. In Figure 8, we plot our modeled T_e against the value of $T_e(\text{[N II]})$ measured by CHAOS directly from the auroral line detections. For the most stringent case, where we allow a variable f_{ion} that depends on $[\text{S III}]/[\text{S II}]$ and employ direct method techniques to measure $12+\log(\text{O}/\text{H})$, we measure a scatter between the two T_e values of ~ 660 K. This scatter is only a factor of 1.5 times larger than the median uncertainty (450 K) reported for $T_e(\text{[N II]})$. Assuming a fixed $f_{\text{ion}}=0.97$ (the median for the CHAOS sample) increases the scatter by almost a factor of two (860 K). Applying a variable f_{ion} prescription and instead using the strong line S calibration metallicity prescription results in a scatter of ~ 900 K. As might be expected, adopting both of these changes, to assume a fixed $f_{\text{ion}}=0.97$ and using the S calibration prescription, results in even larger scatter (~ 950 K). Our final test case is to assume a fixed $f_{\text{ion}}=0.97$ and metallicity for each galaxy. This worst case scenario has a scatter of ~ 1100 K, which is smaller than the uncertainty quoted for 20% of the CHAOS measurements, and still clearly retains the correlation between modeled and directly measured T_e . All of these approaches demonstrate a relatively large systematic offset of 100–300 K between the direct method and “charge-exchange” measurements of T_e , presumably reflecting apertures biases that affect lines with significant radial extent and ionization structure (e.g. $[\text{S II}]$, $[\text{S III}]$ and $[\text{O I}]$, $[\text{O II}]$, $[\text{O III}]$).

This set of tests demonstrate that for this technique the physical motivation is quite robust, able to reproduce reliable T_e values in the range 6,000–10,000 K with an estimated uncertainty of ~ 600 K for integrated H II regions under reasonable assumptions (as outlined in Section 4.3). These also justify our choice of adopting the variable prescription for f_{ion} in Equation 15 that relies on changes in $[\text{S III}]/[\text{S II}]$. The worst-case scenario test, with a fixed $12+\log(\text{O}/\text{H})$ for each galaxy, demonstrates that this technique is not strongly dependent on small changes in metallicity ($\sim < 0.1$ dex) for each region. Our result is specifically calibrated against strong-line metallicities measured using the Pilyugin & Grebel (2016) S calibration, which itself is empirically calibrated against direct method metallicities, and can not account for larger (up to ~ 0.3 dex) offsets sometimes found between different prescriptions. This discrepancy in the absolute abundance scale presents a long standing challenge facing strong line abundance prescriptions that has been much discussed in the literature (Kewley & Ellison 2008; Kewley et al. 2019).

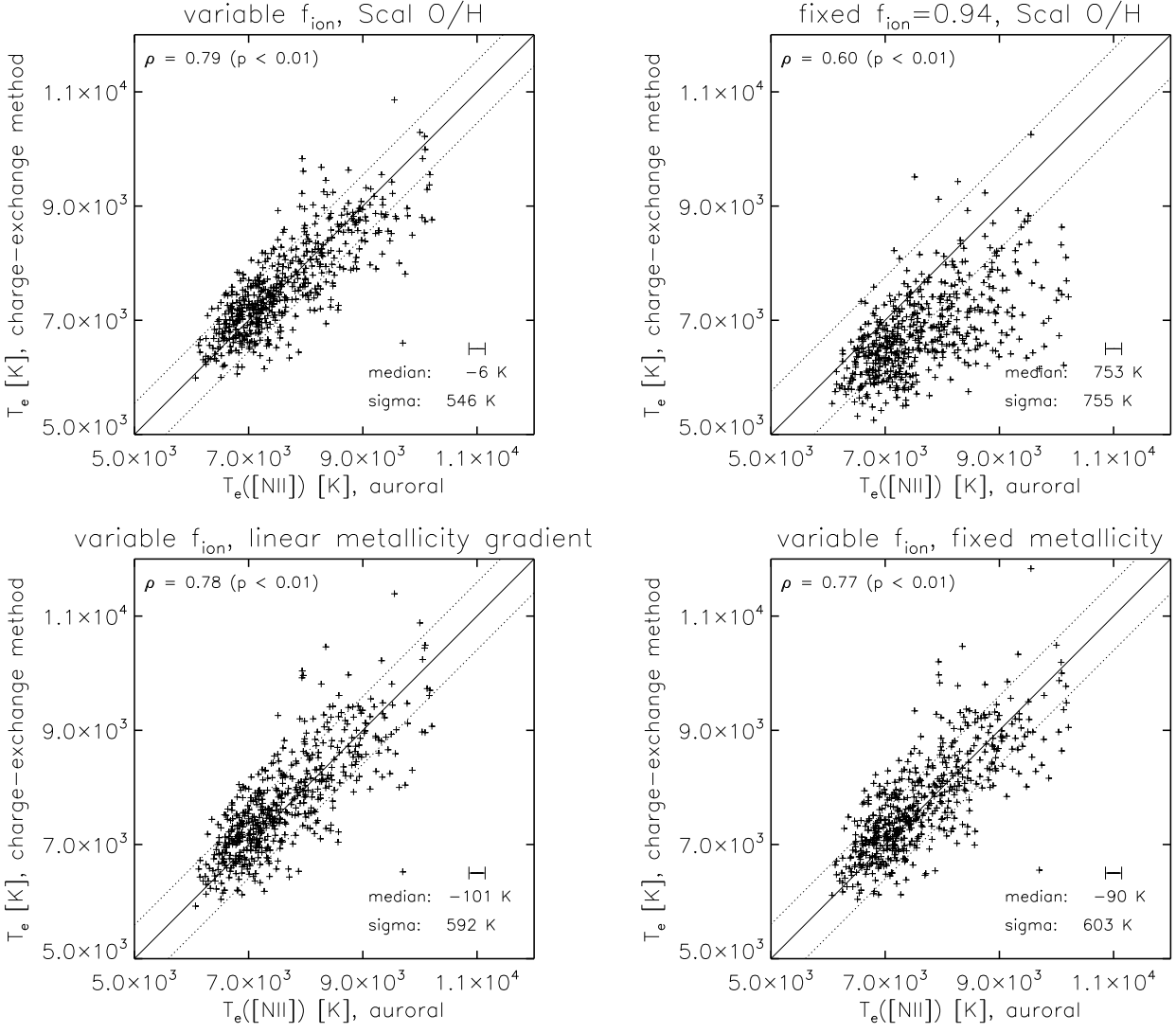


Fig. 7. Comparison of the modeled T_e as a function of the T_e measured within PHANGS-MUSE using the [N II] $\lambda 5755$ auroral line. Each panel makes different assumptions about how the value of f_{ion} or $12+\log(\text{O}/\text{H})$ are calculated. For each panel we show a one-to-one relation (solid line) and 1σ relative scatter (dotted lines), as well as the Spearman's rank correlation coefficient (ρ). Top left: we demonstrate our adopted method (Section 4.3), where we use our empirical prescription for f_{ion} (Equation 15) and metallicities calculated from the strong line Scal method. We recover high correlations ($\rho=0.79$) and systematic agreement within 6 K, with a scatter of 546 K. Relaxing various assumptions in our model increases the scatter. Top right: Assuming a fixed $f_{\text{ion}}=0.94$ (the median for the PHANGS-MUSE sample) produces significantly higher scatter (~ 755 K) and clear deviations from the one-to-one relation. Bottom panels: We apply a variable f_{ion} but relax our derivation of $12+\log(\text{O}/\text{H})$, adopting either a linear radial gradient (left) or a fixed metallicity for each galaxy (right). Both recover high correlation coefficients with moderately increased scatter (~ 600 K). This demonstrates the relative insensitivity to the input metallicity for this charge-exchange method of deriving T_e .

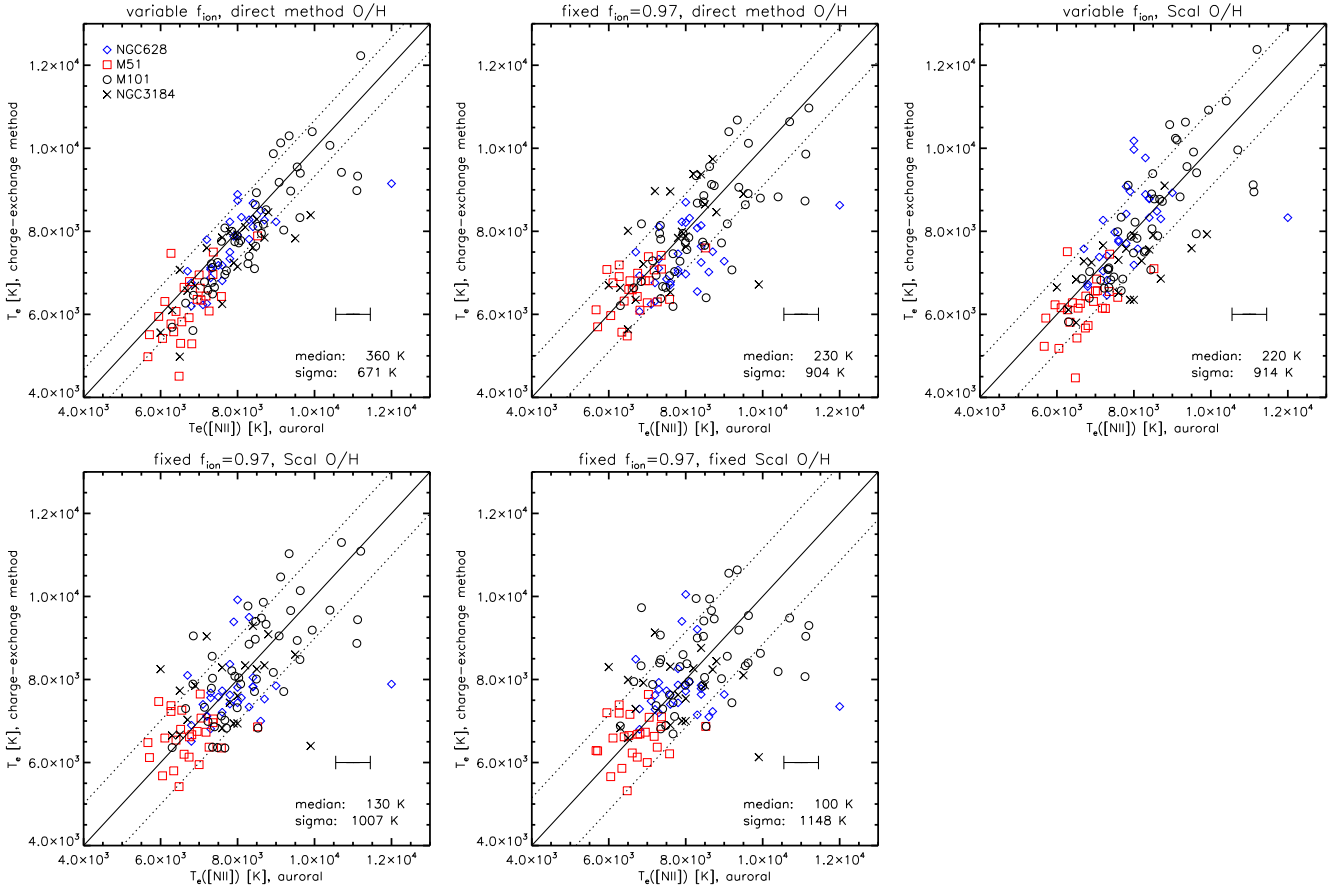


Fig. 8. Comparison of the modeled T_e as a function of T_e measured by CHAOS using the $[\text{N II}] \lambda 5755$ auroral line. Each panel makes different assumption about how the value of f_{ion} and $12+\log(\text{O}/\text{H})$ are calculated. The top left plot represents the best case scenario, where we vary f_{ion} as a function of $[\text{S III}]/[\text{S II}]$ and use metallicities calculated from the direct method. This shows the lowest systematic scatter between T_e values of 662 K. The other two plots on the top row each relax one of the assumptions, either assuming a fixed $f_{\text{ion}}=0.97$ (top center) or a metallicity calculated from strong line techniques (top right). Both have increased scatter of ~ 900 K. The two plots on the bottom row further relax the assumptions, resulting in further inaccuracies. This test includes assuming both fixed $f_{\text{ion}}=0.97$ and a strong line metallicity (~ 950 K; bottom right) and a fixed $f_{\text{ion}}=0.97$ and a fixed global metallicity per galaxy (~ 1100 K; bottom center). A one-to-one relation (solid line) and 1σ scatter (dotted lines) are shown in each plot, and the median and standard deviation are listed. While relaxing our assumptions does result in increased scatter, the overall agreement remains good. We adopt the assumptions that go into the top right figure (variable f_{ion} and strong line $12+\log(\text{O}/\text{H})$) for the model that we apply in this work, as summarized in Section 4.3.

5. Results

We now apply the charge-exchange method to model T_e within the full sample of 24,173 PHANGS-MUSE H II regions.

5.1. Electron temperatures across thousands of H II regions

We find that 4,129 H II regions meet the criteria outlined in Section 4.3, allowing us to compute T_e for nearly a fifth of the H II region sample. This is a factor of ~ 4 times more H II regions than have any auroral line detection, and a factor of ~ 8 times more H II regions than have direct detection of the [N II] $\lambda 5755$ line. The limiting factor for ~ 2000 of the regions is the requirement that the emission lines be detected with sufficient contrast against the surrounding DIG background, and for ~ 5000 H II regions [S III]/[S II] is too low. Another ~ 5000 H II regions meet neither criteria. The remaining ~ 7000 targets do not have sufficient S/N in all lines necessary.

With hundreds of measurements per galaxy, we show two dimensional maps of T_e across four example galaxies (Figure 9). NGC 1672 and NGC 1365 both have previously identified azimuthal variations in their abundance distribution (Ho et al. 2017; Kreckel et al. 2019), as identified using strong line methods, with increased metallicities along the spiral arms. We similarly observe decreased T_e in the H II regions located along the spiral arm ridges, supporting that result (see also Ho et al. 2019), although the effect is less pronounced. NGC 4254 shows a much more flocculent spiral pattern, and the T_e measurements more uniformly sample the disk. NGC 628 hosts a two arm spiral pattern without a bar or strong bulge component, and exhibits a clear gradient in T_e with galactocentric radius.

Figure 10 quantifies the scatter in T_e as a function of scale within all of our maps. Measuring the variation in T_e across 500 pc or 3 kpc scales around each H II region, relative to the mean local value at each position, we find that the probability density function reveals systematically smaller scatter on small physical scales. To perform this calculation, we consider the variation between neighboring regions only when 5 or more H II regions are clustered on 500 pc or 3 kpc scales. We measure a standard deviation of ~ 500 K at 500 pc scales, and ~ 800 K at 3 kpc scales. To test the null hypothesis, that all regions temperatures are uncorrelated, we shuffle all values of T_e and repeat this calculation (dotted lines). This test erases the trend with physical scale and results in a broader distribution. This small scale homogeneity in the T_e distribution reflects the spatial scales relevant to mixing, as also recently determined from strong line methods (Kreckel et al. 2020; Li et al. 2021; Metha et al. 2021; Williams et al. 2022).

In Figure 11 we show the radial gradient in T_e for each of the 19 galaxies. All galaxies show positive gradients, reflecting an expected negative metallicity gradient (Figure 12), such as is typically observed across nearby galaxy samples (Pilyugin et al. 2014). In four galaxies (NGC 1300, NGC 1365, NGC 1566, NGC 4535), significant (~ 900 – 1000 K) scatter is seen in these radial trends, in excess of the uncertainty intrinsic to the method (~ 600 K). This could be indicative of particularly large azimuthal abundance variations in these galaxies, which was also conclusively shown for two of these galaxies in interpolated metallicity maps (Williams et al. 2022).

5.2. Why does this even work?

There are a few crucial assumptions that go into this model (see also Section 2). This model compares the [O I] and H α line emis-

sion, however considering the ionization structure within a nebula (Figure 13) it is clear that these emission lines arise from different regions, with H α emitted predominantly throughout the interior while [O I] is emitted mainly in an outer shell. For this work, we are assuming that T_e is uniform across both the H α and [O I] emitting regions, as is shown in our Cloudy modeling (orange line, Figure 13). At sufficiently high spatial resolution, it would be possible to resolve the internal nebular structure and compare [O I] and H α emission arising from the same parcel of gas, more directly ensuring that this assumption is true, but this is beyond what is possible given our ~ 50 pc physical resolution. This condition of uniform T_e and co-spatial [O I] and H α emission is also likely true in the diffuse ionized gas (e.g. Reynolds et al. 1998).

This method also assumes that the gas is photoionized, and contributions from shocks are negligible. The [O I]/H α ratio is quite sensitive to shock excitation (Allen et al. 2008), spanning two orders of magnitude at constant metallicity and different shock velocities. Therefore, we expect the observed ratio of [O I]/H α to change significantly in the presence of shocks. This is directly observed in supernova remnants (Kopsacheili et al. 2020), and in general we note that the observational locus of “star-forming regions” is not well-represented by models in the [O I] BPT diagram (e.g. Law et al. 2021). How much of this discrepancy is due to the diffuse ionized gas (DIG), and the source of excitation for that diffuse emission, remains an active field of research (Belfiore et al. 2022). Our PHANGS-MUSE nebular catalog has attempted to minimize the impact of other ionizing sources by selecting peaks in H α , using the BPT diagnostic cuts, and having a high contrast against the DIG. We further require our emission lines to be detected with 50% contrast against the DIG. Finally, we attempt to minimize the possibility of shock contributions by employing BPT diagnostic cuts, as described in Section 3.2.

Finally, an essential step in our method is our ability to infer f_{ion} in an independent way from the available strong-lines. We find the strongest correlation with [S III]/[S II] (Figure 1), a robust tracer of the ionization parameter. This begs the question, why is the ionization fraction related to the ionization parameter (q)? Here we consider principally the incident ionization parameter, as seen by the inner edge of the nebula. By definition, $q = \frac{Q(H^0)}{4\pi R^2 n_H}$ (Equation 13), and $f_{\text{ion}} = n_{H^+}/n_H$ (Equation 4). Assuming case B, $Q(H^0)$ could be expressed as $Q(H^0) \simeq \alpha_B \int n_e n^+ dV$, where α_B is the recombination rate coefficient. Assuming a H II region as a thin sphere (a common approximation), we can write that $dV = 4\pi R^2 dl$, where l is the thickness of the shell. Thus, $q \sim \alpha_B \frac{n_e n^+ l}{n_H} \sim \alpha_B f_{\text{ion}} n_e l$, and we find that $q \propto f_{\text{ion}}$ at constant l and n_e . However, we must keep in mind for this argument that this is f_{ion} measured over the full nebula, and not just over the [O I] region in the outer shell.

The remarkable success of this charge-exchange method for deriving T_e in comparison with ~ 500 H II regions in the PHANGS-MUSE sample that have direct auroral line constraints (Figure 7) demonstrates that the spatial averaging over the entire H II region does not invalidate this method. Crucially, as we show through more detailed Cloudy modeling in Section 5.3, this simplistic assumption does not seem to invalidate our derived dependency of f_{ion} on [S III]/[S II], but in fact appears to reduce the scatter in this relation.

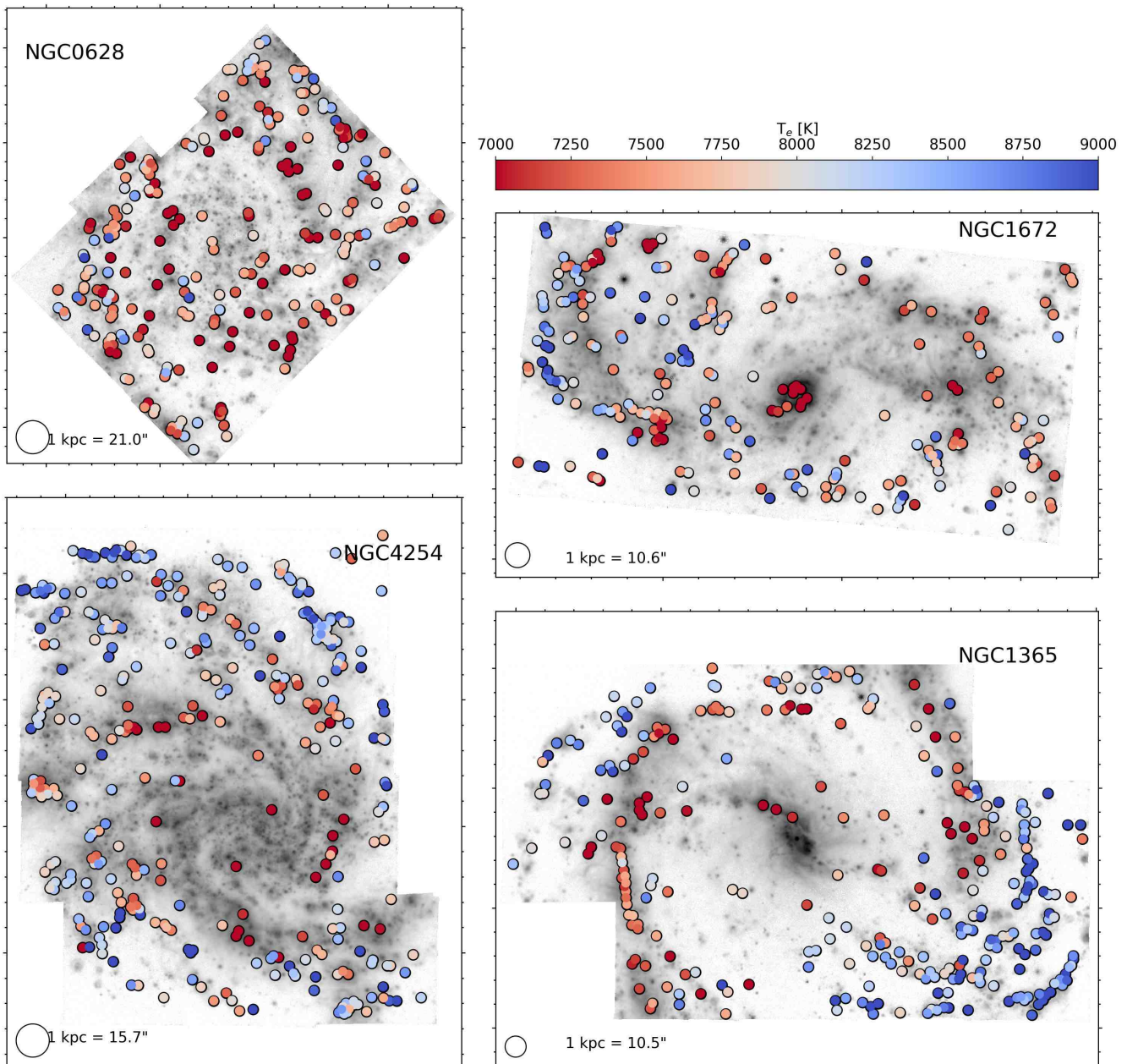


Fig. 9. Mapping electron temperatures within H II regions across four of the PHANGS-MUSE galaxies (NGC 1672, NGC 1365, NGC 4254, NGC 628). Coverage is not just limited to spiral arms, but samples the full inner star-forming disks in our sample of galaxies. NGC 1365 (Ho et al. 2017) and NGC 1672 (Kreckel et al. 2019; Ho et al. 2019) have both reported azimuthal abundance variations, with enhanced abundances along the spiral arms, which is supported by decreased T_e along the eastern arms in both galaxies. The more flocculent galaxy NGC 4254 and the bar-free grand design spiral galaxy NGC 628 both show some tentative azimuthal trends but the connection with spiral structure is more tenuous. Small scale < 1 kpc homogeneity in the temperature distribution is reminiscent of the trends for more uniform metallicity on small scales reported in Kreckel et al. (2020) for these targets.

5.3. Comparison of our f_{ion} relation with models

Crucial to the success of this technique is our ability to infer f_{ion} directly from the $[\text{S III}]/[\text{S II}]$ line ratio. While we establish this empirically through comparison with the PHANGS-MUSE and CHAOS H II regions (Section 4.2 and Figure 6), we here explore how such a relation might emerge from theoretical models.

We compute a set of Cloudy models (Ferland et al. 2017) for the properties of ionizing clusters and nebulae covering the same

parameter space as in the observed sample. To start, we cross-match our catalog of PHANGS-MUSE H II regions with measured auroral lines to a catalog of the stellar associations detected within PHANGS-HST imaging (Lee et al. 2022, Scheuermann et al. in prep). These stellar associations have been identified using a watershed method applied to the NUV and V-band images, and their key parameters (stellar mass, age, reddening) have been inferred from SED modeling (Larson et al. in prep). We identify 150 objects with a one-to-one correspondence between an H II

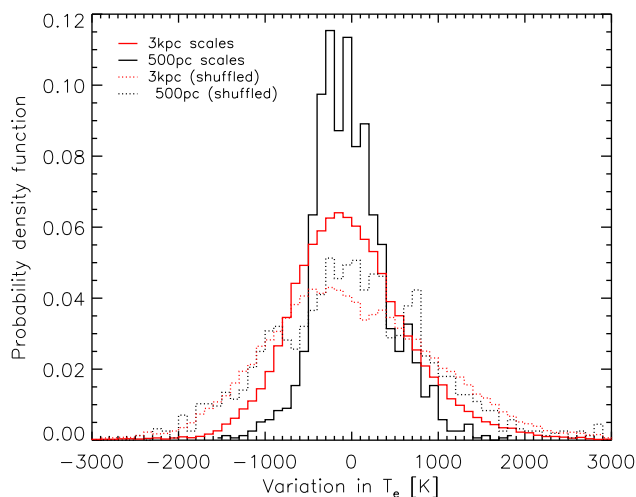


Fig. 10. The probability density function of the variations in T_e at 500 pc (black) and 3 kpc (red) sampling scales across all galaxies in the sample. We perform this calculation around each H II region, relative to the mean local value at each position. We require at least five H II regions be located within the relevant sampling scale length, to minimize biases due to low number statistics. Across all galaxies, we measure a standard deviation of ~ 500 K at 500 pc scales and ~ 800 K at 3 kpc scales. To test the null hypothesis, that all region temperatures are uncorrelated, we shuffle all values of T_e and repeat this calculation (dotted lines).

region and a stellar association, where we can be fairly certain that the identified stellar association is powering the ionization of the H II region. These 150 matched objects have a median age of ~ 3 Myr and a median stellar mass of $\sim 10^4 M_\odot$, and we can further constrain properties such as size (R), gas-phase metallicity ($12 + \log(\text{O}/\text{H})$) and electron density (n_e) as shown in Figure 14. This cross-matched sample was used to establish the range of model parameters that we explore.

We run Cloudy v17.02 models (using the PYCLOUDY package, Morisset 2013) consisting of a spherical gas cloud surrounding an ionizing source and take the following range in parameters based on the observations: constant density $n_{\text{H}} \approx n_e = 20, 90$ and 300 cm^{-3} ; metallicity $12 + \log(\text{O}/\text{H}) = 7.99, 8.47$ and 8.69 (that corresponds to $Z/Z_\odot = 0.2, 0.6$ and 1.0 assuming the Solar relative abundance of elements from Grevesse et al. 2010); inner radius of the shell $R = 0$ (cloud), 15, 28, 40 pc. We also varied the volume filling factor in the range of 0.1 – 1.0, but it has a neglectable effect on the output models. As an ionizing source we used the spectra produced by Starburst99 (Leitherer et al. 2014) for instantaneous star formation, a Kroupa initial mass function (Kroupa 2001), and Geneva stellar evolution tracks which include rotation (metallicity $Z = 0.014$, Ekström et al. 2012, and $Z = 0.002$, Georgy et al. 2013)¹ for clusters with total stellar mass $\log(M_*/M_\odot) = (3.5, 4.5, 5.5)$ and age of 0.6 Myr plus 1 to 9 Myr with steps of 1 Myr. Each Cloudy model has been iterated until convergence, and the termination criterium was reaching the lowest temperature $T_e = 4000$ K. We can then compute integrated properties across the full model, including line fluxes, line ratios, and f_{ion} . As follows from the bottom-right panel of Figure 14, the resulting grid of Cloudy and Starburst99 models produces the same range of $H\alpha$ luminosities as is seen for

¹ We used used stellar evolution tracks for $Z = 0.002$ ($\sim 0.15Z_\odot$) only for the nebulae with $12 + \log(\text{O}/\text{H}) = 7.99$; for the other nebulae we used $Z = 0.014$ ($\sim Z_\odot$).

the reference H II regions selected from PHANGS-MUSE, however the exact distributions do not match each other because the model parameter space is regularly sampled (in contrast to the observational data).

We derive the integrated value of f_{ion} from the Cloudy models as the ratio of number densities averaged over a nebula volume:

$$f_{\text{ion}} = \frac{\langle n(\text{H}^+) \rangle}{\langle n(\text{H}) \rangle} = \frac{\int n_{\text{H}^+}(r)r^2 dr}{\int n_{\text{H}}(r)r^2 dr}, \quad (16)$$

where $n_{\text{H}^+}(r)$ and $n_{\text{H}}(r)$ are the ionized and total hydrogen number density in each zone of the modelled nebula, and r is the radius of the corresponding zone. We can easily calculate these integrals from the computed Cloudy models and thus obtain f_{ion} characterizing the whole nebula.

As seen in the left-hand panel of Figure 15, the range of values for f_{ion} calculated in the models agrees very well with the measurements obtained from observations, but with large scatter. This scatter in the f_{ion} relation as a function of $[\text{S III}]/[\text{S II}]$ is significantly larger than in the observational measurements, driven mostly by differences in the age of the ionizing cluster. To some extent, the reduced scatter for the observational data could be a result of an observational bias, as many of the stellar associations have very young ages (~ 1 Myr, Figure 14). However, we see clear offsets between the youngest Cloudy models and the empirical relation derived in Figure 6. Note also that similar correlation between f_{ion} and $[\text{S III}]/[\text{S II}]$ exists also at the scales of individual zones (radii) of the models (central panel) where f_{ion} is not affected by the truncation criteria of a model or by its geometry.

5.3.1. Assumption of co-spatial [O I] and $H\alpha$

One of the limitation of the charge-exchange method (as described in Section 5.2) is that Equation 6 should only work for [O I] and $H\alpha$ emitted co-spatially within a nebula, but in unresolved observations we collect line emission from the whole nebula. Thus, our measurement of $[\text{O I}]/H\alpha$ differs from the value corresponding to the area where the charge-exchange process occurs. This, in turn, should lead to deviations between the f_{ion} empirically calibrated for this work and f_{ion} when considering only the [O I] emitting region. From our Cloudy models, we directly estimate how significant this deviation is. For that we calculate f_{ion} following the method used with our observational data – we measure the integrated value of [O I]/ $H\alpha$, adopt the input metallicity of the model, and derive f_{ion} using Equation 6 assuming $T_e = T_e([\text{N II}])$ as obtained directly from the model. In Figure 15 (right) we show that the discrepancy between the empirical correlation and the Cloudy models is significantly reduced when we calculate f_{ion} in the same way as we did with the observational data. We note in particular that the scatter in f_{ion} vs. $[\text{S III}]/[\text{S II}]$ is very similar to that for observational data, and now the empirical relation correlates with the Cloudy models for youngest age (see right-hand panel of Figure 15), consistent with the expected observational bias.

The fact that the ‘true’ values of f_{ion} do not agree with those obtained from Equation 6 directly follows from the limitation of this equation when applied to unresolved H II regions. Indeed, we can invert our use of Equation 6, and use it to compute the expected [O I]/ $H\alpha$ based on our Cloudy models. The values of [O I]/ $H\alpha$ that we compute from Equation 6 assuming the ‘true’ f_{ion} derived from Equation 16 are significantly overestimated in comparison with the ‘true’ line ratios from the Cloudy

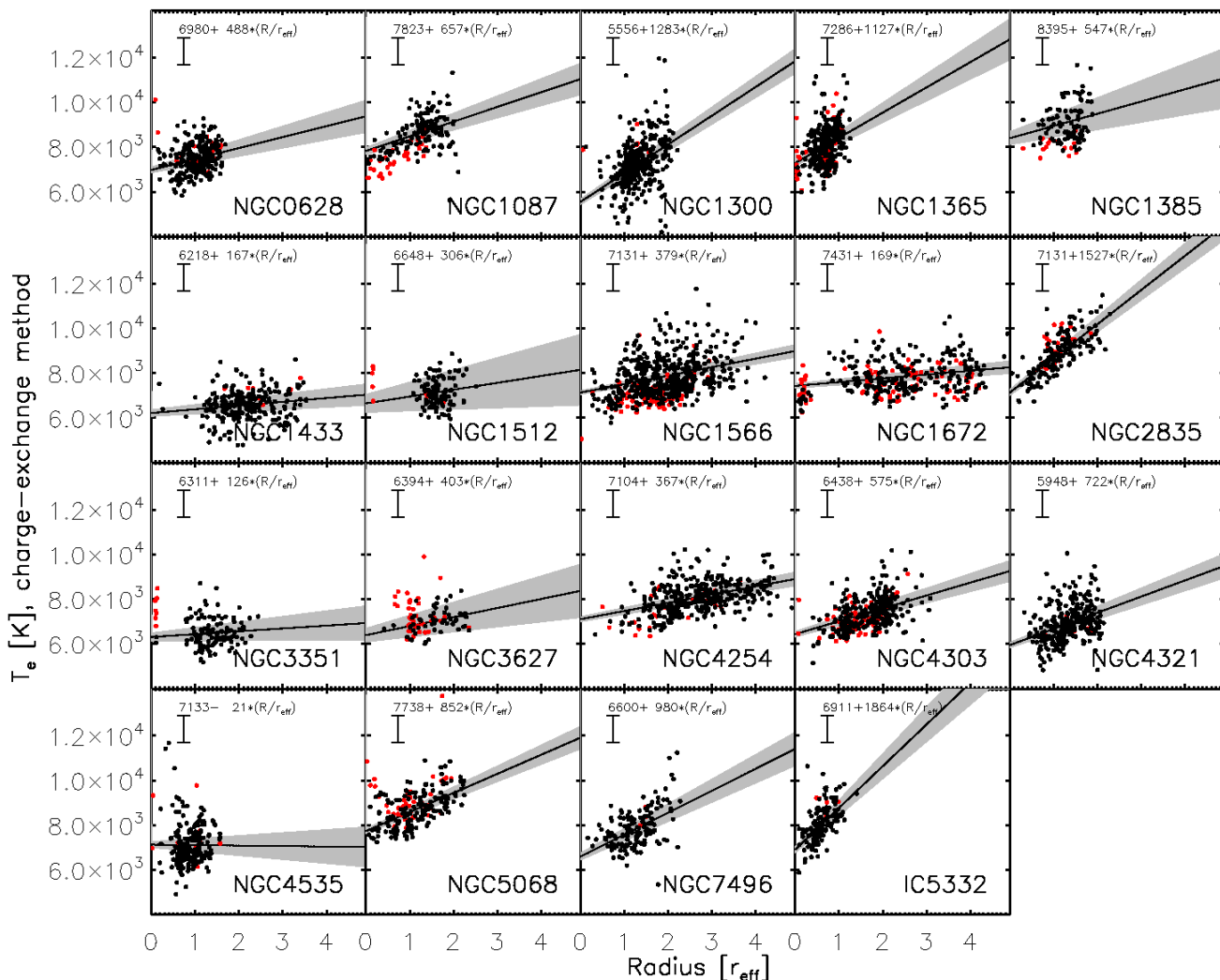


Fig. 11. The radial gradient in T_e for each of the PHANGS-MUSE galaxies. Red points show T_e determined from auroral line measurements, while black points show T_e measured using the charge exchange method. Positive slopes show general agreement with the expected flat to negative metallicity gradients reported in these and other nearby galaxies (Pilyugin et al. 2014; Kreckel et al. 2019). A linear fit is shown for each galaxy, with the fit parameters listed in the top of each plot. The grey band indicates the uncertainty in the linear fit, accounting for 600 K systematic uncertainty in the T_e measurements.

models (left-hand panel of Figure 16). At the same time, Equation 6 reproduces well the $[\text{O I}]/\text{H}\alpha$ ratio when it is applied to the individual local zones of the Cloudy models (central panel of Figure 16).² We show in Appendix A that a revised version of Equation 6 that considers the volumetric differences in the $[\text{O I}]$ and $\text{H}\alpha$ emitting zones is more complicated (Equation A.23) and cannot be solved for unresolved H II regions. However, we can test the impact introducing a volumetric correction using the Cloudy models. Integrating the term ξ' , dependent on the local f_{ion} over all Cloudy zones, we obtain values for $[\text{O I}]/\text{H}\alpha$ that are in very good agreement with those in the output of the Cloudy models (right-hand panel of Figure 16).

From this analysis we conclude that Equation 6, which is fundamental to our method, is valid for both resolved and unresolved nebulae, but for latter it is necessary to weigh f_{ion} according to the volumes occupied by the $[\text{O I}]$ and $\text{H}\alpha$ emitting

² We believe the small departures from the 1-to-1 relation might be caused by the differences in the atomic data used in the Cloudy models compared to our calculations (see Appendix A), and by the violation of our assumption of a uniform distribution of T_e .

zones instead of using the ‘true’ f_{ion} . By definition, the values of f_{ion} derived from $[\text{O I}]/\text{H}\alpha$ and used in the right-hand plot of Figure 15 already include these weights, and that is why they disagree with the ‘true’ f_{ion} (Figure 16, left). The empirically defined values of f_{ion} obtained by Equation 15 are weighted as the ionization structure in sulphur encodes some of these volumetric effects, and as a result our relation intrinsically corrects for this potential bias.

As the goal of the presented method is to obtain the measurements of electron temperature, we carry out a final test by comparing the values of $T_e([\text{N II}])$ derived from Equation (6) with the output of our Cloudy models. As follows from Figure 17, in general, both values are indeed in agreement if we use the observationally-defined calibration of f_{ion} (Equation 15), or solve Equation A.23 on a zone-by-zone basis. Moreover, the empirical calibration shows even better agreement with the 1-to-1 relation in the high T_e regime. Note, however, that the method significantly underestimates T_e for the regions ionized by older star clusters. In summary, while we have shown the theoretical limitations of this approach, based on the underlying physical

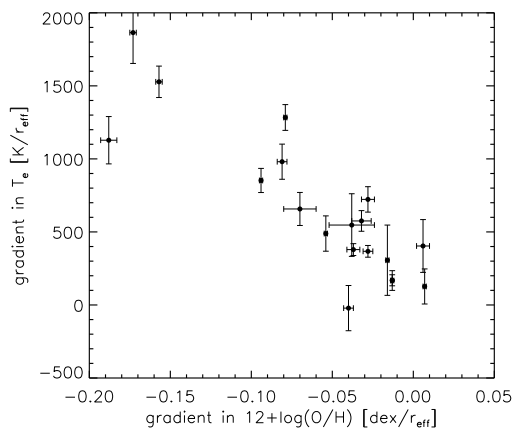


Fig. 12. The slope of the radial gradient in T_e as a function of the slope of the radial gradient in $12+\log(\text{O}/\text{H})$ (Santoro et al. 2022) for each PHANGS-MUSE galaxy. Positive slopes in temperature correspond (as expected) to negative slopes in metallicity, as metal-rich gas is more efficient at cooling.

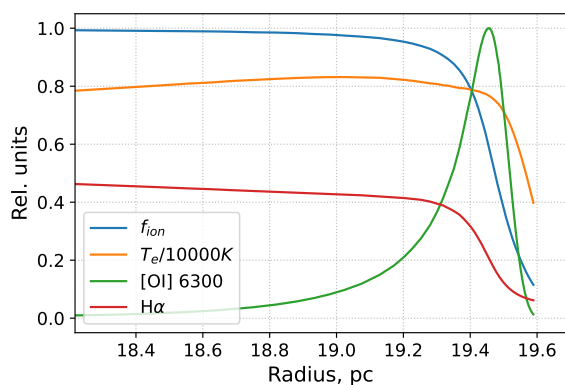


Fig. 13. Cloudy modeling of the interior structure of a typical H II region. The $\text{H}\alpha$ emission (red) traces fairly closely the ionization fraction (f_{ion} , blue) as a function of radius, while the $[\text{O I}]$ (green) is predominantly emitted in the outer shell of the nebula. In this way, it is apparent that very little of the $\text{H}\alpha$ emission is co-spatial with the $[\text{O I}]$, a key assumption in our model. At the outer edge of the nebula, the intensity of $[\text{O I}]$ rapidly drops together with the electron temperature T_e (orange).

mechanisms governing the charge-exchange process, we further demonstrate that our empirical calibration based on integrated nebulae sufficiently accounts for the unresolved volumetric effects.

5.3.2. Age as a secondary parameter

Based on the remarkable visual agreement between the Cloudy models and observed data when using f_{ion} inferred from $[\text{O I}]/\text{H}\alpha$ in the models, and the matched biases regarding spatial averaging, we choose to use this modeled value of f_{ion} to independently derive a relation between f_{ion} and $[\text{S III}]/[\text{S II}]$. We apply our empirical calibration from Equation 15 to the Cloudy models. As shown in Figure 18 (left), this relation shows relatively good agreement at high $f_{\text{ion}} > 0.9$, but a clear secondary dependence on age. While the age of an H II region is difficult to constrain observationally, strong correlations are seen in models with the equivalent width (EW) of $\text{H}\alpha$ (Leitherer et al. 2014). We use the EW output from the Cloudy models, and include this secondary

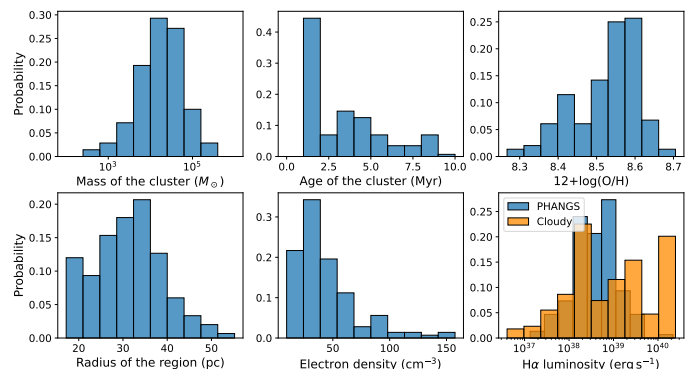


Fig. 14. Distributions of the observed properties for 150 H II regions with measured auroral lines and a 1-to-1 correspondence with a young stellar association (Scheuermann et al. in prep). These ranges in cluster mass, stellar cluster age, gas-phase metallicity, size and electron density are used to establish the parameter range used in our Cloudy models. The bottom-right panel shows the distribution of the reddening-corrected $\text{H}\alpha$ luminosity in both the observational sample and computed Cloudy models.

dependence to perform a third order polynomial fit to Figure 15 (right) in order to derive the following functional form:

$$f_{\text{ion}} = 0.992 + 0.0076 \cdot (x + 0.8295 - 0.731y + 0.148xy)^3, \quad (17)$$

where again $x = \log_{10}([\text{S III}]/[\text{S II}])$ and $y = \log_{10}(\text{EW}(\text{H}\alpha))$. In Figure 18 (right), we see that this successfully removes the secondary dependence on age.

There is one remaining complication in our comparison of the modeled and observed empirical relations. According to the Cloudy models, we find that $\text{EW}(\text{H}\alpha) \approx 1815 \text{ \AA}$ at an age of 1 Myr, however based on our observations we find $\text{EW}(\text{H}\alpha) \approx 126 \text{ \AA}$ for the same aged nebulae that show a 1-to-1 correspondence with the HST stellar associations (Larsen et al. in prep, Scheuermann et al. in prep). This offset between modeled and observed EW has been previously reported (Morisset et al. 2016), and it can be a consequence of the large escape fraction of ionizing radiation from H II regions, or of the significant contribution of underlying old stellar population – both factors are not considered in the Cloudy models. Likely we are seeing a combination of both effects, as typical escape fractions are expected to be $\sim 50\%$ (Oey & Kennicutt 1997; Doran et al. 2013; Belfiore et al. 2022), which alone is insufficient to account for the difference. To first order a simple scaling is possible whereby we ‘convert’ the observed $\text{EW}(\text{H}\alpha)$ to the modeled $\text{EW}(\text{H}\alpha)$ at this fixed reference age of 1 Myr, such that the variable y in Equation 17 is replaced with $y = \log_{10}(\text{EW}(\text{H}\alpha)_{\text{obs}} \cdot 1815/126)$.

We apply this prescription to the PHANGS-MUSE H II region catalog and show the resulting values in Appendix B.1. Directly comparing the $\text{EW}(\text{H}\alpha)$ measurements with the Cloudy derived model for f_{ion} (Figure 19), it is apparent that while the general trends are in agreement, the exact values of $\text{EW}(\text{H}\alpha)$ between the models and observations are not in good enough agreement that we can rely on the calibration. However, it demonstrates the potential in future work for improving our T_e measurements by including age sensitive indicators (such as $\text{EW}(\text{H}\alpha)$) in the prescription, which is not generally done in the literature.

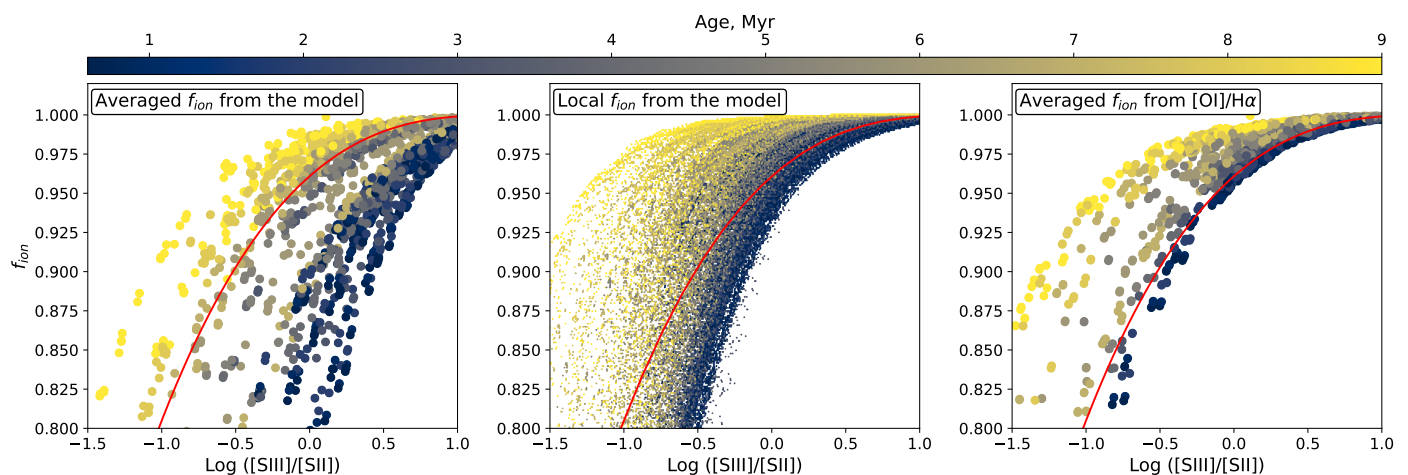


Fig. 15. The relation between f_{ion} and $[\text{S III}]/[\text{S II}]$ based on the Cloudy models. On the left-hand panel the value of f_{ion} is obtained directly from the model (as $\langle n(\text{H}^+) \rangle / \langle n(\text{H}) \rangle$), while on the right-hand panel it was derived as in the observations (Equation (6)) based on the integrated values of $[\text{O I}]/\text{H}\alpha$ metallicity and electron temperature $T_e([\text{N II}])$. The central panel shows $f_{\text{ion}} = n(\text{H}^+)/n(\text{H})$ in individual zones of the models. The colors on all panels correspond to the age of the ionizing cluster, and the red curve is the empirical relation derived from the observational data (Equation 15). Spatially integrating across the entire line emitting region clearly reduces the scatter in this relation, and brings the model results into better agreement with the empirical relation.

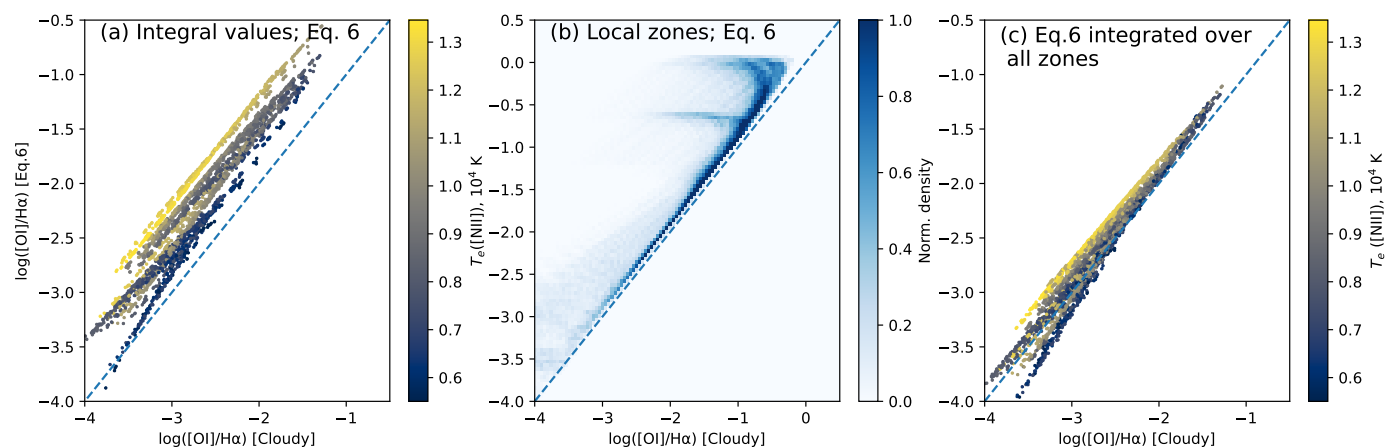


Fig. 16. Validation of Equation 6 using our Cloudy models. Panel (a): Comparison of $[\text{O I}]/\text{H}\alpha$ calculated with this relation assuming the mean f_{ion} (Equation 16) to the Cloudy output. Panel (b): The same comparison, but applied to the individual local zones in the Cloudy models. Here f_{ion} corresponds to the local values of $n(\text{H}^+)/n(\text{H})$. Panel (c): The same test, but applied to results using Equation A.23 that are accounting for variations of f_{ion} and the spatial extent of the $[\text{O I}]$ and $\text{H}\alpha$ emitting zones.

6. Conclusions

We develop a new method that exploits the charge-exchange between oxygen and hydrogen to infer the electron temperature, T_e , within H II regions using only strong emission lines. This single temperature corresponds to the $[\text{O I}]$ and $\text{H}\alpha$ emitting zone. This method requires three parameters: the $[\text{O I}]/\text{H}\alpha$ line ratio, the gas-phase metallicity $12+\log(\text{O}/\text{H})$ and the ionization fraction f_{ion} . Using observations from the CHAOS survey (Berg et al. 2020), where auroral line observations of T_e are available for ~ 150 H II regions, we demonstrate that f_{ion} correlates with changes in various strong line ratios. We show that the strongest correlation is with $[\text{S III}]/[\text{S II}]$, tracing changes in ionization parameter. However, due to aperture biases, we cannot derive an empirical relation from this data set alone.

We then use 840 H II regions from the PHANGS-MUSE survey that have auroral line detections of $[\text{N II}] \lambda 5755$ to develop an empirical relation between f_{ion} and $[\text{S III}]/[\text{S II}]$ for line fluxes measured across integrated H II regions. Due to limitations of our calibration sample and concerns about the contribution from

diffuse ionized gas, where strong-lines like $[\text{S II}]$ and $[\text{O I}]$ are strongly emitted, we conservatively apply this method only to H II regions that have $[\text{S III}]/[\text{S II}] > 0.5$ and a contrast of more than 50% against the local DIG background. With these restrictions, we recover $T_e([\text{N II}])$ to within ~ 600 K. This uncertainty only increases slightly when we assume a fixed metallicity for each galaxy, demonstrating that this charge-exchange method is not strongly sensitive to the exact determination of metallicity.

Of the $\sim 24,000$ H II regions in the PHANGS-MUSE nebular catalog (Santoro et al. 2022), we are then able to apply this technique to model T_e for a total of 4,129 H II regions, ~ 4 times more than have direct auroral line detections. We recover positive radial temperature gradients that reflect the expected negative metallicity gradients. Four galaxies show a scatter in their radial temperature gradient of ~ 1000 K, well beyond the uncertainties of the method and likely tracing azimuthal variations in the metallicity at fixed radius.

While some of the assumptions that go into this method would not appear to be met, particularly the assumption that the

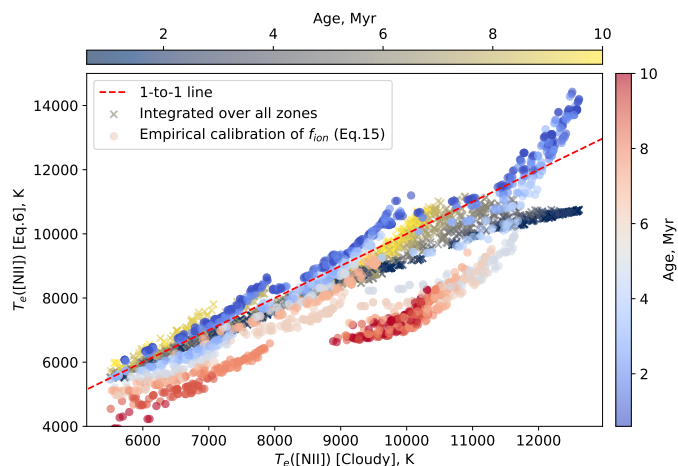


Fig. 17. A validation of the resulting values for T_e based on the Cloudy models. Crosses shows the values of T_e ([N II]) obtained from the volumetric version of Equation 6, which accounts for variations in f_{ion} and the spatial extent of the [O I] and $H\alpha$ emitting zones (Equation A.23). Circles represent the T_e ([N II]) values yielded by Equation 6 assuming the empirical calibration of f_{ion} (by Equation 15). The calculated values are compared with the ‘true’ T_e ([N II]) from the Cloudy models. The symbol colour encodes the age of the ionizing cluster. Both data sets show generally good agreement with the 1-to-1 relation, but the empirical calibration significantly underestimate T_e for old regions. Note that for the empirically-calibrated results we show only the models with $\log([\text{OI}]/H\alpha) \geq -3$ and $-1 \geq \log([\text{SIII}]/[\text{SII}]) \leq -0.7$ that correspond to the values obtained in our observations (see, e.g., Figures 3 and 6). The prominent ‘tails’ towards higher T_e for the empirically-calibrated values correspond only to those regions where $\log([\text{SIII}]/[\text{SII}]) > 0.5$ – only a few such regions were used for calibration of Equation 15, thus the calibration is less certain for H II regions with the highest ionization parameters.

[O I] and $H\alpha$ emitting regions have matched electron temperatures, and ideally are co-spatial, we carry out a set of Cloudy models to explore the robustness of our method and in particular to test the empirically derived relation between f_{ion} and $[\text{S III}]/[\text{S II}]$. We find that by integrating over the full H II region, our models actually recover the tight observed correlation between f_{ion} and $[\text{S III}]/[\text{S II}]$, with a significant secondary dependence on the age of the ionizing stellar cluster. We parameterize this age dependence by changes in the equivalent width of $H\alpha$, which shows qualitatively similar agreement to the observed data but significant quantitative differences in the measured values, particularly for $\text{EW}(H\alpha)$. For this reason, we prefer the empirical calibration for f_{ion} , but note that $\text{age}/\text{EW}(H\alpha)$ represents a promising additional parameter to consider when deriving accurate H II region temperatures and metallicities.

This novel method for determining T_e demonstrates the remarkable potential arising from these new catalogs containing 100–1000s of H II regions with uniform data, as well as future planned surveys (e.g. SIGNALS, Rousseau-Nepton et al. 2019; SDSS-V/LVM, Kollmeier et al. 2017; AMASE, Yan et al. 2020). While this method is physically motivated, there is clearly an exciting potential for the application of machine learning approaches to these data sets.

Acknowledgements. We thank the referee for their comments, which improved our analysis of the subtleties of this method. We thank Jose Eduardo Mendez Delgado for his comments and input. This work was carried out as part of the PHANGS collaboration. Based on observations collected at the European Southern Observatory under ESO programmes 1100.B-0651, 095.C-0473, and 094.C-0623 (PHANGS–MUSE; PI Schinnerer), as well as 094.B-0321 (MAGNUM; PI Marconi), 099.B-0242, 0100.B-0116, 098.B-0551 (MAD; PI Carollo)

and 097.B-0640 (TIMER; PI Gadotti). KK, OE and FS gratefully acknowledge funding from the German Research Foundation (DFG) in the form of an Emmy Noether Research Group (grant number KR4598/2-1, PI Kreckel). SCOG and RSK acknowledge support from the DFG via SFB 881 ‘‘The Milky Way System’’ (Project-ID 138713538; sub-projects B1, B2 and B8) and from the Heidelberg cluster of excellence EXC 2181-390900948 ‘‘STRUCTURES: A unifying approach to emergent phenomena in the physical world, mathematics, and complex data’’, funded by the German Excellence Strategy. RSK furthermore thanks for funding from the European Research Council via the ERC Synergy Grant ECOGAL (grant 855130). TGW acknowledges funding from the European Research Council (ERC) under the European Union’s Horizon 2020 research and innovation programme (grant agreement No. 694343).

References

- Allen, M. G., Groves, B. A., Dopita, M. A., Sutherland, R. S., & Kewley, L. J. 2008, *ApJS*, 178, 20
- Anand, G. S., Lee, J. C., Van Dyk, S. D., et al. 2021, *MNRAS*, 501, 3621
- Azimlu, M., Marciniak, R., & Barmby, P. 2011, *AJ*, 142, 139
- Bacon, R. et al. 2010, in *Proc. SPIE*, Vol. 7735, Ground-based and Airborne Instrumentation for Astronomy III, 773508
- Baldwin, J. A., Phillips, M. M., & Terlevich, R. 1981, *PASP*, 93, 5
- Balser, D. S., Wenger, T. V., Anderson, L. D., & Bania, T. M. 2015, *ApJ*, 806, 199
- Barklem, P. S. 2007, *A&A*, 462, 781
- Barnes, A. T., Glover, S. C. O., Kreckel, K., et al. 2021, *MNRAS*, 508, 5362
- Belfiore, F., Santoro, F., Groves, B., et al. 2022, *A&A*, 659, A26
- Berg, D. A., Pogge, R. W., Skillman, E. D., et al. 2020, *ApJ*, 893, 96
- Berg, D. A., Skillman, E. D., Croxall, K. V., et al. 2015, *ApJ*, 806, 16
- Croxall, K. V., Pogge, R. W., Berg, D. A., Skillman, E. D., & Moustakas, J. 2015, *ApJ*, 808, 42
- Croxall, K. V., Pogge, R. W., Berg, D. A., Skillman, E. D., & Moustakas, J. 2016, *ApJ*, 830, 4
- Dong, R. & Draine, B. T. 2011, *ApJ*, 727, 35
- Dopita, M. A., Kewley, L. J., Sutherland, R. S., & Nicholls, D. C. 2016, *Ap&SS*, 361, 61
- Doran, E. I., Crowther, P. A., de Koter, A., et al. 2013, *A&A*, 558, A134
- Dors, Jr., O. L., Krabbe, A., Hägele, G. F., & Pérez-Montero, E. 2011, *MNRAS*, 415, 3616
- Draine, B. T. 2011, *Physics of the Interstellar and Intergalactic Medium* (Princeton University Press)
- Ekström, S., Georgy, C., Eggenberger, P., et al. 2012, *A&A*, 537, A146
- Emsellem, E., Schinnerer, E., Santoro, F., et al. 2022, *A&A*, 659, A191
- Ferland, G. J., Chatzikos, M., Guzmán, F., et al. 2017, *Rev. Mexicana Astron. Astrofis.*, 53, 385
- Georgy, C., Ekström, S., Eggenberger, P., et al. 2013, *A&A*, 558, A103
- Grevesse, N., Asplund, M., Sauval, A. J., & Scott, P. 2010, *Ap&SS*, 328, 179
- Hausen, N. R., Reynolds, R. J., & Haffner, L. M. 2002, *AJ*, 124, 3336
- Ho, I. T. 2019, *MNRAS*, 485, 3569
- Ho, I. T., Kreckel, K., Meidt, S. E., et al. 2019, *ApJ*, 885, L31
- Ho, I. T., Seibert, M., Meidt, S. E., et al. 2017, *ApJ*, 846, 39
- Hummer, D. G. & Storey, P. J. 1987, *MNRAS*, 224, 801
- Kauffmann, G., Heckman, T. M., Tremonti, C., et al. 2003, *MNRAS*, 346, 1055
- Kepley, A. A., Chomiuk, L., Johnson, K. E., et al. 2011, *ApJ*, 739, L24
- Kewley, L. J. & Dopita, M. A. 2002, *ApJS*, 142, 35
- Kewley, L. J. & Ellison, S. L. 2008, *ApJ*, 681, 1183
- Kewley, L. J., Heisler, C. A., Dopita, M. A., & Lumsden, S. 2001, *ApJS*, 132, 37
- Kewley, L. J., Nicholls, D. C., & Sutherland, R. S. 2019, *ARA&A*, 57, 511
- Klessen, R. S. & Glover, S. C. O. 2016, *Saas-Fee Advanced Course*, 43, 85
- Kollmeier, J. A., Zasowski, G., Rix, H.-W., et al. 2017, *arXiv e-prints*, arXiv:1711.03234
- Kopsacheili, M., Zezas, A., & Leonidaki, I. 2020, *MNRAS*, 491, 889
- Kreckel, K., Ho, I. T., Blanc, G. A., et al. 2020, *MNRAS*, 499, 193
- Kreckel, K., Ho, I. T., Blanc, G. A., et al. 2019, *ApJ*, 887, 80
- Kroupa, P. 2001, *MNRAS*, 322, 231
- Lang, P., Meidt, S. E., Rosolowsky, E., et al. 2020, *ApJ*, 897, 122
- Law, D. R., Ji, X., Belfiore, F., et al. 2021, *ApJ*, 915, 35
- Lee, J. C., Whitmore, B. C., Thilker, D. A., et al. 2022, *ApJS*, 258, 10
- Leitherer, C., Ekström, S., Meynet, G., et al. 2014, *ApJS*, 212, 14
- Leroy, A. K., Schinnerer, E., Hughes, A., et al. 2021, *ApJS*, 257, 43
- Li, Z., Krumholz, M. R., Wisnioski, E., et al. 2021, *arXiv e-prints*, arXiv:2104.14807
- Luisi, M., Anderson, L. D., Bania, T. M., et al. 2018, *PASP*, 130, 084101
- Luidiana, V., Morisset, C., & Shaw, R. A. 2015, *A&A*, 573, A42
- Maiolino, R. & Mannucci, F. 2019, *A&A Rev.*, 27, 3
- Mannucci, F., Belfiore, F., Curti, M., et al. 2021, *MNRAS*, 508, 1582
- McKee, C. F. & Ostriker, E. C. 2007, *ARA&A*, 45, 565
- Metha, B., Trenti, M., & Chu, T. 2021, *MNRAS[arXiv:2109.03390]*

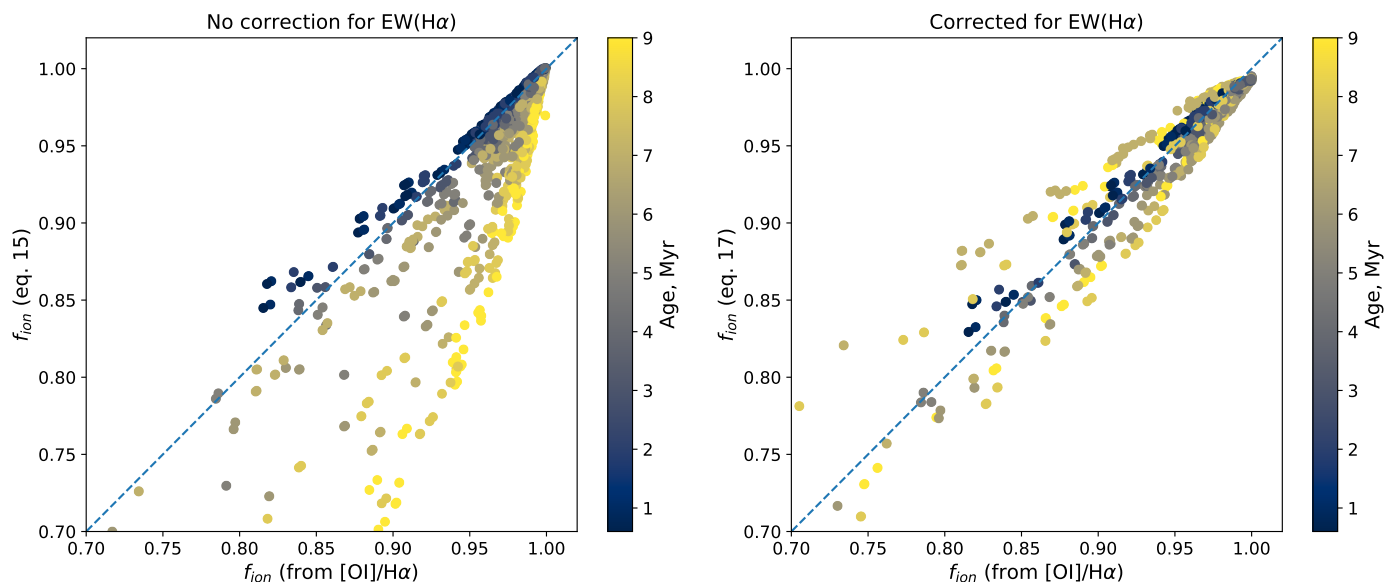


Fig. 18. A comparison of the cloudy modeled f_{ion} measured from $[\text{OI}]/\text{H}\alpha$ with what is derived using a fit based on $[\text{S III}]/[\text{S II}]$ (as in Figure 15, right). The left-hand panel depends only on $x = \log_{10}([\text{S III}]/[\text{S II}])$ while the right-hand panel includes a secondary dependence on age as traced by the equivalent width of $\text{H}\alpha$, as $y = \log_{10}(\text{EW}(\text{H}\alpha))$. Both plots are colored by the age of the ionizing stellar cluster, and correcting for this secondary dependence significantly improves the agreements between the fit and the value for f_{ion} in the cloudy models.

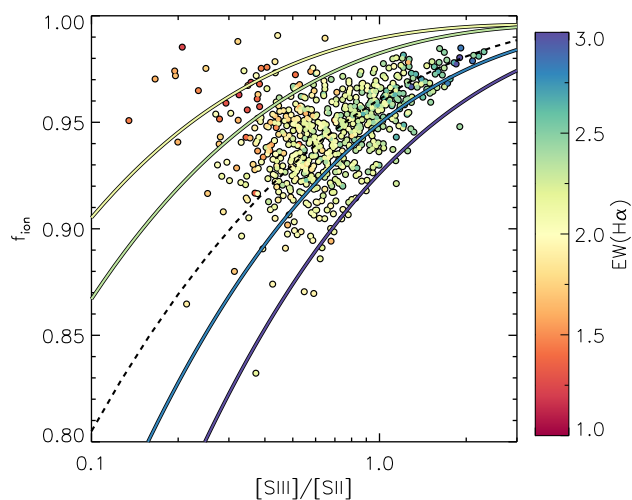


Fig. 19. A direct comparison of the observed f_{ion} as a function of $[\text{S III}]/[\text{S II}]$ within the PHANGS-MUSE H II regions with the age-dependent fit resulting from the cloudy models (colored lines, Equation 17). The colors correspond to $\text{EW}(\text{H}\alpha)$, and for the cloudy model fits they have been scaled as described in the text in order to account for the large quantitative discrepancy between model and observation. The observed data shows a clear gradient, indicating that age trends do play an important role in driving the scatter in this relation. The empirical fit (dashed line) shows good qualitative agreement with the age-dependent cloudy model fit, supporting our choice of this empirical calibration. However, while the trends are consistent, a significant offset is seen between the $\text{EW}(\text{H}\alpha)$ measurements and the predicted values, preventing a straightforward application of our model-driven calibrations to the data.

- Pilyugin, L. S. & Grebel, E. K. 2016, MNRAS, 457, 3678
Pilyugin, L. S., Grebel, E. K., & Kniazev, A. Y. 2014, AJ, 147, 131
Pineda, J. L., Horiuchi, S., Anderson, L. D., et al. 2019, ApJ, 886, 1
Pogge, R. W., Atwood, B., Brewer, D. F., et al. 2010, in Society of Photo-Optical Instrumentation Engineers (SPIE) Conference Series, Vol. 7735, Ground-based and Airborne Instrumentation for Astronomy III, ed. I. S. McLean, S. K. Ramsay, & H. Takami, 77350A
Reynolds, R. J., Hausen, N. R., Tufte, S. L., & Haffner, L. M. 1998, ApJ, 494, L99
Rosolowsky, E. & Simon, J. D. 2008, ApJ, 675, 1213
Rousseau-Nepton, L., Martin, R. P., Robert, C., et al. 2019, MNRAS, 489, 5530
Sánchez-Menguiano, L., Sánchez Almeida, J., Muñoz-Tuñón, C., et al. 2019, arXiv e-prints, arXiv:1904.03930
Santoro, F., Kreckel, K., Belfiore, F., et al. 2022, A&A, 658, A188
Schlafly, E. F. & Finkbeiner, D. P. 2011, ApJ, 737, 103
Tayal, S. S., Zatsarinny, O., & Sossah, A. M. 2019, ApJS, 242, 9
Thilker, D. A., Braun, R., & Walterbos, R. A. M. 2000, AJ, 120, 3070
Tielens, A. G. G. M. 2010, The Physics and Chemistry of the Interstellar Medium (Cambridge University Press)
Wenger, T. V., Balsaer, D. S., Anderson, L. D., & Bania, T. M. 2019, ApJ, 887, 114
Williams, T. G., Kreckel, K., Belfiore, F., et al. 2022, MNRAS, 509, 1303
Yan, R., Bershady, M. A., Smith, M. P., et al. 2020, in Society of Photo-Optical Instrumentation Engineers (SPIE) Conference Series, Vol. 11447, Society of Photo-Optical Instrumentation Engineers (SPIE) Conference Series, 114478Y
Zhao, J.-H., Anantharamaiah, K. R., Goss, W. M., & Viallefond, F. 1996, ApJ, 472, 54

- Mingozi, M., Belfiore, F., Cresci, G., et al. 2020, A&A, 636, A42
Morisset, C. 2013, pyCloudy: Tools to manage astronomical Cloudy photoionization code
Morisset, C., Delgado-Inglada, G., Sánchez, S. F., et al. 2016, A&A, 594, A37
Oey, M. S. & Kennicutt, R. C., J. 1997, MNRAS, 291, 827
Osterbrock, D. E. & Ferland, G. J. 2006, Astrophysics of gaseous nebulae and active galactic nuclei (University Science Books)

Appendix A: Derivation of line emissivity relation

The emissivity of [O I] $\lambda 6300$ transition can be written as:

$$\epsilon_{\text{OI}} = \Delta E_{\text{OI}} R_{\text{OI}} n(\text{O}^0) n(e^-), \quad (\text{A.1})$$

where R_{OI} is the excitation rate coefficient for the $^3\text{P}-^1\text{D}$ transition and ΔE_{OI} is the energy of the transition. If we assume that the electrons come primarily from ionized hydrogen, then $n(e^-) \approx n(\text{H}^+)$ and we can instead write this as

$$\epsilon_{\text{OI}} = \Delta E_{\text{OI}} R_{\text{OI}} n(\text{O}^0) n(\text{H}^+). \quad (\text{A.2})$$

The $\text{H}\alpha$ emissivity due to H^+ recombination can be written as

$$\epsilon_{\text{H}\alpha} = \Delta E_{\text{H}\alpha} R_{\alpha} n(e^-) n(\text{H}^+) \approx \Delta E_{\text{H}\alpha} R_{\alpha} n(\text{H}^+)^2, \quad (\text{A.3})$$

where R_{α} is the rate coefficient for the production of $\text{H}\alpha$ photons during recombination (i.e. the product of the recombination rate and the fraction of recombinations resulting in $\text{H}\alpha$) and $\Delta E_{\text{H}\alpha}$ is the energy of $\text{H}\alpha$. Taking the ratio of the emissivities yields:

$$\frac{\epsilon_{\text{OI}}}{\epsilon_{\text{H}\alpha}} = \frac{\Delta E_{\text{OI}} R_{\text{OI}} n(\text{O}^0)}{\Delta E_{\text{H}\alpha} R_{\alpha} n(\text{H}^+)}. \quad (\text{A.4})$$

We now want to eliminate the dependence on the O^0 fraction in favour of a dependence on the H^+/H ratio and the total elemental abundance of oxygen. To do this, we use the fact that the balance between O^0 and O^+ is set by charge transfer with hydrogen:



If we denote the rate coefficient for the forward reaction (producing O^+) as k_f and the rate coefficient for the reverse reaction as k_r , then chemical equilibrium between these two reactions implies that

$$k_f n(\text{O}^0) n(\text{H}^+) = k_r n(\text{O}^+) n(\text{H}^0). \quad (\text{A.7})$$

Denoting the total elemental abundance of oxygen as $n(\text{O})$, we can use the relation $n(\text{O}^+) = n(\text{O}) - n(\text{O}^0)$ to write this as:

$$k_f n(\text{O}^0) n(\text{H}^+) = k_r [n(\text{O}) - n(\text{O}^0)] n(\text{H}^0). \quad (\text{A.8})$$

Rearranging for $n(\text{O}^0)$ then yields

$$n(\text{O}^0) = n(\text{O}) n(\text{H}^0) \left[\frac{k_f}{k_r} n(\text{H}^+) + n(\text{H}^0) \right]^{-1}. \quad (\text{A.9})$$

The difference between the ionization potentials of hydrogen and oxygen is very small and at high temperatures we can ignore it and assume that the energy change in the forward and reverse reactions is zero. In this case, the ratio of the forward and reverse rate coefficients is simply the ratio of the statistical weights of the products, i.e.

$$\frac{k_f}{k_r} = \frac{g_{\text{O}^+} g_{\text{H}^0}}{g_{\text{O}^0} g_{\text{H}^+}}. \quad (\text{A.10})$$

With $g_{\text{O}^0} = 9$, $g_{\text{O}^+} = 4$, $g_{\text{H}^0} = 2$ and $g_{\text{H}^+} = 1$, this yields $k_f/k_r = 8/9$. Therefore,

$$n(\text{O}^0) = n(\text{O}) n(\text{H}^0) \left[\frac{8}{9} n(\text{H}^+) + n(\text{H}^0) \right]^{-1}, \quad (\text{A.11})$$

$$= n(\text{O}) r \left[\frac{8}{9} + r \right]^{-1}, \quad (\text{A.12})$$

where $r = n(\text{H}^0)/n(\text{H}^+)$. Substituting this into the ratio of the emissivities then yields

$$\frac{\epsilon_{\text{OI}}}{\epsilon_{\text{H}\alpha}} = \frac{\Delta E_{\text{OI}} R_{\text{OI}} n(\text{O})}{\Delta E_{\text{H}\alpha} R_{\alpha} n(\text{H}^+)} \frac{r}{8/9 + r}. \quad (\text{A.13})$$

Finally, we can use the fact that

$$n(\text{H}) = n(\text{H}^+) + n(\text{H}^0) = n(\text{H}^+) [1 + r] \quad (\text{A.14})$$

to write this as

$$\frac{\epsilon_{\text{OI}}}{\epsilon_{\text{H}\alpha}} = \frac{\Delta E_{\text{OI}} R_{\text{OI}}}{\Delta E_{\text{H}\alpha} R_{\alpha}} r^{\xi} \frac{n(\text{O})}{n(\text{H})}, \quad (\text{A.15})$$

where $\xi = (1 + r)/(8/9 + r)$. Comparing this with Equation 1 in Reynolds et al. (1998) shows us that they use the following expression for $\Delta E_{\text{OI}} R_{\text{OI}}/\Delta E_{\text{H}\alpha} R_{\alpha}$:

$$\frac{\Delta E_{\text{OI}} R_{\text{OI}}}{\Delta E_{\text{H}\alpha} R_{\alpha}} = 2.63 \times 10^4 \frac{T_4^{1.85}}{1 + 0.605 T_4^{1.105}} \exp\left(-\frac{2.284}{T_4}\right), \quad (\text{A.16})$$

where $T_4 = T/10000$ K.

For our updated calculation, we have computed R_{OI} for large number of different temperatures by numerically integrating the cross-section data³ from Barklem (2007) and have then fit a function to the resulting rate. The best fit that we have found is the following:

$$R_{\text{OI}} = 9.54 \times 10^{-10} f_{\text{OI}}(T) \exp\left(-\frac{2.284}{T_4}\right), \quad (\text{A.17})$$

where

$$f_{\text{OI}}(T) = \sum_{i=0}^6 a_i T_4^i. \quad (\text{A.18})$$

This fit is accurate to within 3% for temperatures in the range $3000 < T < 30000$ K, but is not guaranteed to give sensible results outside of this temperature range.

Coefficient	Value
a_0	-1.00
a_1	+6.4854011
a_2	-4.17358515
a_3	+1.81446389
a_4	-0.514022051
a_5	+8.39069326 $\times 10^{-2}$
a_6	-5.93343677 $\times 10^{-3}$

Since $\Delta E_{\text{OI}} = 3.155 \times 10^{-12}$, it then follows that:

$$\Delta E_{\text{OI}} R_{\text{OI}} = 3.01 \times 10^{-21} f_{\text{OI}}(T) \exp\left(-\frac{2.284}{T_4}\right). \quad (\text{A.19})$$

For $\text{H}\alpha$, we can use the accurate fit given in Draine (2011) to the data of Hummer & Storey (1987):

$$\Delta E_{\text{H}\alpha} R_{\alpha} = 4\pi j_{\text{H}\alpha} = 3.54 \times 10^{-25} T_4^{-0.942-0.031 \ln T_4}. \quad (\text{A.20})$$

This fit is also accurate to within a few percent in the temperature range of interest. Combining these then yields

$$\frac{\Delta E_{\text{OI}} R_{\text{OI}}}{\Delta E_{\text{H}\alpha} R_{\alpha}} = 8492 \frac{f_{\text{OI}}(T)}{T_4^{-0.942-0.031 \ln T_4}} \exp\left(-\frac{2.284}{T_4}\right), \quad (\text{A.21})$$

³ Available at <https://github.com/barklem/public-data/tree/master/>

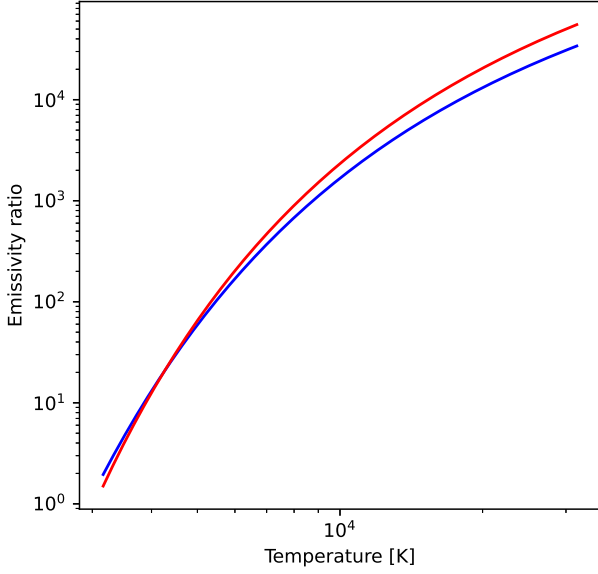


Fig. A.1. A comparison of the emissivity coefficients computed in Section A (red) with the value provided in Reynolds et al. (1998) (blue). For H II region temperatures in the normal range for PHANGS galaxies, the difference is around 20-40%.

and hence

$$\frac{\epsilon_{\text{OI}}}{\epsilon_{\text{H}\alpha}} = 8492 \frac{f_{\text{OI}}(T)}{T_4^{-0.942-0.031 \ln T_4}} \exp\left(-\frac{2.284}{T_4}\right) r \xi \frac{n(\text{O})}{n(\text{H})}. \quad (\text{A.22})$$

A comparison of the relations for $\frac{\Delta E_{\text{OI}}}{\Delta E_{\text{H}\alpha}} \frac{R_{\text{OI}}}{R_{\alpha}}$ provided by Reynolds et al. (1998) and derived here is shown in Figure A.1.

Note that in general, the ratio of the total observed fluxes in [O I] and H α is not equal to the ratio of their emissivities, but can be expressed from the equations above as follows (assuming a uniform T_e across the [O I] and H α emitting zones):

$$\begin{aligned} I([\text{OI}])/I(\text{H}\alpha) &= \frac{\int_{V_{[\text{OI}]}} \epsilon_{\text{OI}} dV}{\int_{V_{\text{H}\alpha}} \epsilon_{\text{H}\alpha} dV} = \\ &= 8492 \frac{f_{\text{OI}}(T)}{T_4^{-0.942-0.031 \ln T_4}} \exp\left(-\frac{2.284}{T_4}\right) \xi' \frac{n(\text{O})}{n(\text{H})} \end{aligned} \quad (\text{A.23})$$

where ξ' depends on the distribution of the hydrogen ionization fraction $f_{\text{ion}} = n(\text{H}^+)/n(\text{H}) = 1/(1+r)$ in the [O I] and H α emitting zones as

$$\xi' = \frac{\int_{V_{[\text{OI}]}} \frac{r}{(1+r)(8/9+r)} dV}{\int_{V_{\text{H}\alpha}} 1/(1+r)^2 dV}. \quad (\text{A.24})$$

Equation (A.23) is equal to Equation A.22 (and thus - to Equation 6) if one assumes that [O I] and H α come from the same zones. We discuss the limitation of this assumption in Section 5.3.1.

Appendix B: Application of the model-based prescription for f_{ion}

As described in Section 5.3, we use a series of Cloudy models to derive f_{ion} as a function of [S III]/[S II] across integrated H II

regions. Given the similarities between the model results and our observations, we explore using the Cloudy models to derive a new prescription for f_{ion} , and improve upon them by adding an age dependence based on variations in EW(H α) (Equation 17).

In this section, we explore how well this model-driven parameterization of f_{ion} applies to our observed PHANGS-MUSE H II regions. For each H II region, we calculate EW(H α) to use as an age tracer. Here, we assume that the stellar continuum is dominated by light from the young stellar population, which may not be the case for low EW(H α) regions. Given the added dependence on age (via inclusion of EW(H α)), we can remove our requirement that [S III]/[S II] > 0.5. We find that this doubles the number of H II regions for which we can apply the charge exchange method to a total of ~ 9000 H II regions, nearly half of all H II regions in the PHANGS-MUSE sample.

In Figure B.1 we compare the charge-exchange method T_e with the T_e derived from auroral line detections. We note that the scatter is significantly increased (~ 1000 K instead of 600 K). Considering only H II regions with EW(H α) > 50 Å significantly reduces this scatter but also limits the total number of H II regions.

In Figure B.2 we plot the radial gradient in T_e for each galaxy. Again, we see that for many of the H II regions at low EW(H α) this prescription for f_{ion} results in particularly large T_e values (10,000–12,000 K).

As this revised parameterization for f_{ion} does not result in improved agreement with $T_e([\text{N II}])$ and results in unphysically high T_e values along the radial gradient, combined with the systematic offsets between modeled and measured EW(H α), we choose in this paper to adopt the empirically calibrated relation for f_{ion} (Equation 15).

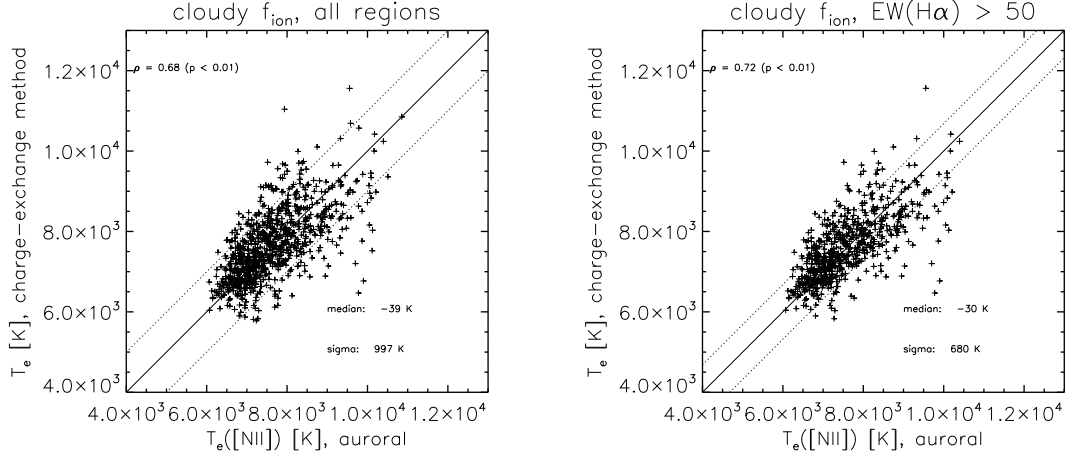


Fig. B.1. A comparison of T_e derived from the charge-exchange method, with $T_e(\text{N II})$, derived from auroral line detections, for H II regions in the PHANGS-MUSE sample. For the charge-exchange method, we use the parametrization of f_{ion} derived from Cloudy models (Equation 17). We find systematically larger scatter (~ 1000 K) compared to the relation in Figure 7, where f_{ion} was empirically calibrated. The scatter is still larger, even when we only consider younger (higher $\text{EW}(\text{H}\alpha)$) H II regions.

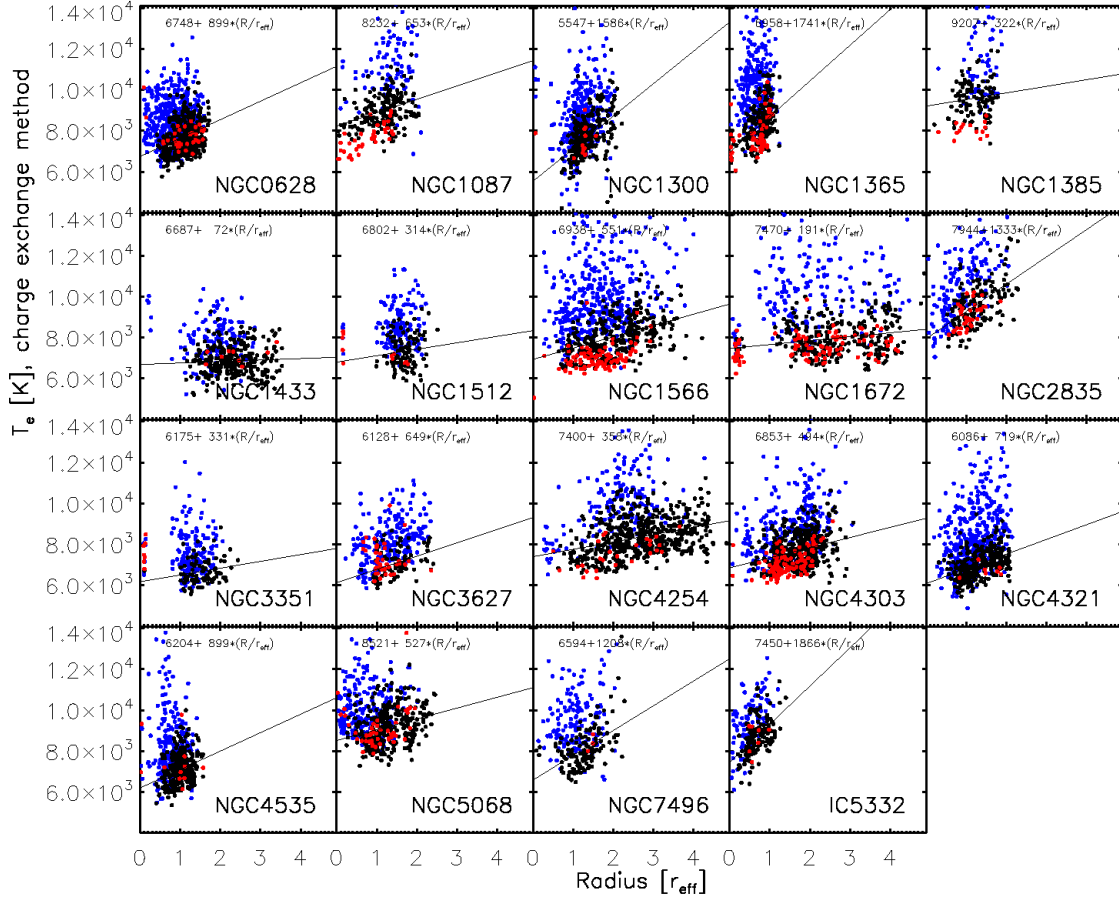


Fig. B.2. Radial gradients in T_e for each galaxy, using f_{ion} parameterized from Cloudy models (Equation 17). H II regions marked in blue have $\text{EW}(\text{H}\alpha) < 50 \text{ \AA}$ a regime poorly sampled by our calibrations and at the extremes of the Cloudy models. These all have systematically higher T_e , suggesting problems with the calibration. H II regions with younger ages (black) show better agreement with the auroral line measurements (red), similar to Figure 11.